

修　士　論　文

題　目 Broadband frequency entangled
 photon generation
 using silicon nitride ring cavities

指導教員 竹内　繁樹　教授

京都大学大学院工学研究科 電子工学専攻

氏名 殷　政浩

令和2年1月31日

Broadband frequency entangled photon generation using silicon nitride ring cavities

Zhenghao Yin

Abstract

Frequency entangled photon source is widely required in a variety of optical quantum technology, including but no limited to quantum key distribution, cluster state quantum computation and quantum metrology etc. In the recent decade, chip-scale entangled photon source has been developed in silicon platform for its robustness, large scalability and COMS technology compatibility. However, due to the intrinsic two-photon absorption and limitation of transparency range, the high-intensity and broadband frequency entangled photon pairs such as one-octave, remains an outstanding challenge.

Here, we report the generation of frequency entangled photon pairs using silicon nitride ring cavities, which is transparent from visible to mid-infrared range and no intensity-dependent absorption. The device design technique is first introduced in the term of phase matching condition. Then, we demonstrate the standard subtractive fabrication and compare mainstream silicon nitride deposition methods. Based on the device transmission, the dispersion evaluation method for broadband frequency entangled photon generation is developed. The quality factor of 5×10^4 is achieved in our device, promising to generate broadband frequency entangled photons in the optical communication band.

Furthermore, we exploit fabless device and success to realize chip-scale frequency entangled photon generation at μW power level. The estimated photon pair generation rate is 15 cps/ μW based on our setup. Furthermore, maximal 46 mode pairs are observed using 24.5 mW pump power, indicating a 106 nm span frequency correlation.

Contents

1	Introduction	1
1.1	Background	1
1.2	Objective	2
1.3	Outline	3
2	Basics of four wave mixing in a ring cavity	4
2.1	Guided-wave optics	4
2.1.1	Waveguide modes	5
2.1.2	Dispersion relation	6
2.2	Ring resonators	7
2.2.1	Coupling condition	8
2.2.2	Spectrum characteristics	8
2.3	Third-order nonlinear optics	10
2.4	Phase matching condition in nonlinear ring resonators	13
3	Device design and dispersion engineering of nonlinear ring cavities	16
3.1	Dispersion compensation	17
3.2	Dispersion engineering using slot structure	18
3.3	Effects of mode crossing	19
3.4	Edge coupling	19
4	Device fabrication of silicon nitride ring resonators	20
4.1	Film deposition	21
4.2	Patterning	21
4.3	ICP etching	22
4.4	Top oxide cladding	22
4.5	Annealing	22
4.6	Chip dicing	23

4.7	Summary	24
5	Device evaluation and dispersion analysis of samples fabricated using various CVD methods	25
5.1	Material properties	25
5.1.1	Ellipsometry	25
5.1.2	Fourier-transform infrared spectroscopy	25
5.2	Device transmission	26
5.2.1	Methods	26
5.2.2	Thermal stability	28
5.2.3	Results	28
5.3	Dispersion analysis	29
5.4	Summary	30
6	Fabless samples via foundries	31
6.1	Fabless process	31
6.2	Device evaluation	32
6.2.1	Coupling evolution	32
6.2.2	Dispersion inversion	32
6.2.3	Comparison of quality factor and dispersion	33
7	Broadband photon pair generation	34
7.1	Methods	35
7.2	Low power photon pair generation	36
7.2.1	Single mode photon flux	36
7.2.2	Coincidence counts of singular mode pair	37
7.3	Pump power dependence	37
7.4	Joint spectral intensity	38
8	Summary	39
Acknowledgements		41
References		42

Chapter 1

Introduction

1.1 Background

Quantum mechanics has not only boosted up the modern science and technology in different disciplines, but also established the cornerstone for future quantum information processing technology. Differing from the past applications of quantum mechanics which only involves the quantization nature, the frontier quantum information processing including but not limited to quantum computation, quantum communication and quantum metrology, exploits the deep-level physics of quantum mechanics, such as quantum superposition and quantum entanglement. Therefore, the fundamental quanta of light—photon—featuring attractive advantages like long coherent time and multiple degrees of freedom (DoF), is a suitable candidate in the research of quantum computation and quantum communication.

Furthermore, entanglement between photon pairs which originates from the nonlocality of quantum mechanics, can be easily realized using nonlinear bulk crystals. While in the term of DoF, much of research up to now focuses on the polarization and path entanglement approaches and very little attention has been paid to frequency entanglement, whose basis is continuous and infinite in hilbert space. Moreover, the previous research shows that frequency entangled photon pairs can be utilized not only in wavelength division multiplexing quantum key distribution [1] but also promising to transfer quantum information in future quantum networks [2]. An extra example for quantum computation is cluster state encoded by frequency [3]. Therefore, frequency entangled photon plays a powerful and general role for optical quantum information processing.

Nevertheless, large scale realization of frequency entanglement requires hundreds of free-space optical components, especially the nonlinear crystals, which

challenges robust manipulation of generated quantum states. Besides, in recent applications of quantum metrology, quantum optical coherent tomography (QOCT), the broadband frequency entanglement [4] is also urgent.

To improve both scalability and robustness, chip-scale full-optical routine has been developed for optical quantum information processing [5–7]. A conventional material candidate is silicon on insulator (SOI), since it is CMOS compatible and supplied by silicon wafer manufacturers. Much of research up to date reported not only frequency [8] but also path and time-bin encoded quantum state in this platform [9, 10]. Other materials like lithium niobate, aluminum nitride and high-index contrast doped glass (HICDG) [11] are also developed and show various advantages, but special fabrication technology is required.

1.2 Objective

However, due to energy band structure, silicon suffers from two photon absorption and stimulated Raman scattering at high pump power regime [12], thus it is no able to perform high-intensity and broadband frequency conversion. An alternative material is silicon nitride, which is transparent from visible to near infrared range and characterizes no obvious two photon absorption. A simple comparison of these two materials is shown in Table 1.1. Recently, single photon pair generation from visible to optical communication band is reported[13].

Similar to silicon, in the silicon nitride waveguide, third-order optical nonlinearity is dominant and leads to spontaneous four wave mixing in sub-micron scale without influence of two-photon absorption. To enhance the optical nonlinear interaction, the all-pass type ring resonator is adopted where the light is coupled inside from a adjacent bus waveguide.

Shown in Figure 1.1, as continuous wave laser is launched at the cavity resonant mode, the ring made of nonlinear material is strongly driven and leads to frequency broadening intracavity. As a result, other resonant modes are excited sequentially, i.e. photons are generated spontaneously and collectively. Indeed, this progress is governed by phase matching condition in nonlinear optics. In our research, by carefully optimizing the device geometry, broadband phase matching condition can be realized. Finally, all the photon pair generation events are detected by single photon detectors and verified by the coincident counting.

1.3 Outline

The following chapters are sequentially divided in several topics.

- In Chapter 2, basic theory concerning nonlinear ring resonators is to be introduced, covering guided optics, ring cavities, nonlinear optics and phase matching condition of four wave mixing.
- In Chapter 3, design and optimization of ring resonator structure are discussed, especially the dispersion compensation method.
- In Chapter 4, we employ standard subtractive fabrication process, from film deposition to lithography, then dry etching and top oxide layer cladding. Here, three different chemical vapor deposition (CVD) methods are compared.
- In Chapter 5, the device fabricated above is evaluated in the term of device transmission and dispersion. The influence of CVD methods is discussed.
- In Chapter 6, due to the fabrication imperfection during our process, fabless device is involved and evaluated in the same way.
- In Chapter 7, we focus on the photon pair generation experiments using fabless device.
- In Chapter 8, all the topics are summarized and some extensive outlooks are given.

Chapter 2

Basics of four wave mixing in a ring cavity

The way how light travels in a chip-scale is remarkably different the way in free-space. In the sub-micron scale, the electromagnetic wave can only propagate in a fewer cycles due to the constraint of material boundaries. However, since atoms and molecules are much smaller, the refractive index is unchanged, as well as the reflection, interference and diffraction.

Based on these facts, in order to perform quantum optics experiments *at the bottom*, first, we shall confine the light propagation in a specific waveguide. On the other hand, thanks to modern laser technology, nonlinear optics is involved and give birth to optical frequency conversion. To enhance these nonlinear optical phenomena, we adopt the cavity structure and achieve sizable control.

In this chapter, we briefly introduce the guided wave theory and then move the cavity structure, ring resonators. Next, the nonlinear optics, in particular third-order nonlinear processes, is discussed in the following section. Although the quantum nature of photon pair generation distinct from the classical theory, all the physics mentioned above are necessary to analyse our essential research object, the silicon nitride ring resonators.

2.1 Guided-wave optics

In an ideal optical waveguide, the core layer and the cladding layer are usually composed of two different materials, where the refractive index is larger in the core. As an analogue of optical fibers, only in the higher index region can the

light propagate, and meanwhile dissipate in a wavelength scale in the lower index region.

Usually, we assume the core and the cladding layer are made of nonmagnetic (magnetic permeability $\mu = \mu_0$) and dielectric material (conductivity $\sigma = 0$). Furthermore, we neglect the nonlinear response of the polarization of electric field ($\mathbf{P} \simeq \epsilon_0 \chi \mathbf{E}$).

Since the waveguide in numerous research objects, is deposited or sputtered using chemical or physical methods, the uneven density in the waveguide layer can not be negligible. Hence, the propagation equation derived from Maxwell's equation is

$$(\nabla_{\perp}^2 + k^2 n^2 - \beta^2) \mathbf{E} = -(\nabla_{\perp} + i\beta \hat{\mathbf{z}}) (\mathbf{E}_{\perp} \cdot \nabla_{\perp} \ln n^2) \quad (2.1)$$

where \perp denotes the transverse component, $\nabla_{\perp}^2 = \nabla_x^2 + \nabla_y^2$. And k, n, β are the wave vector in vacuum, refractive index and propagation constant, respectively. While, with the negligible film anisotropy, Equation 2.1 can be approximated into

$$(\nabla_{\perp}^2 + k^2 n^2 - \beta^2) \mathbf{E} = 0 \quad (2.2)$$

This is the normal Helmholtz equation, indicating the relation between propagation constant β and material refractive index, i.e. chromatic dispersion.

Next, the boundary conditions determining the solution to Eqn. 2.2, arise from the Maxwell's equations as well.

$$\begin{aligned} \hat{\mathbf{n}} \cdot (\mathbf{E}_a - \mathbf{E}_b) &= 0 \\ \hat{\mathbf{n}} \times (\mathbf{H}_a - \mathbf{H}_b) &= 0 \end{aligned}$$

which is the continuity condition of both electric and magnetic field at all dielectric material interfaces. Here, $\hat{\mathbf{n}}$ is the normal direction at the material boundary and the subscript a, b denote different regions.

2.1.1 Waveguide modes

In the case of channel waveguides, the index discontinuity from both vertical and horizontal sides can be decomposed into two sets of independent and complete conditions, i.e. the horizontal boundary condition and vertical boundary condition, with the discontinuity on the waveguide corners neglected. In other words, approximately the equation has two independent particular solutions, which is the

mathematical origin of transverse electric (TE) modes and transverse magnetic (TM) modes.

Hence, we can study the eigenequation by selecting only one set of boundary condition, as used in the effective index method. For example, in a planar waveguide yielding $d^2/dy^2 = 0$ ¹ shown in Figure 2.1, the TE mode features $E_x = 0$ and consider only y -component,

$$\frac{d^2E_y}{dx^2} + (k^2 n^2 - \beta^2) E_y = 0 \quad (2.3)$$

and E_y is continuous at $x = \pm d/2$, where d is the thickness of core layer.

For the region $|x| > d/2$, the light evanesces at x -direction at rate κ and in contrast, in the region of core layer, the light performs like stationary wave, denoting with k_x . By substituting these conditions, phase continuity is achieved between two interface

$$2k_x d = m\pi + 2 \arctan(\kappa/k_x) \quad (2.4)$$

where m is the index of stationary wave. The second term can be treated as the Goos-Hänchen phase shift. Overall, the waveguide modes characterize that the phase shall maintain itself with an $m\pi$ shift along with the shift at the boundaries.

In the case of TM modes, the eigen equation is

$$2k_x d = m\pi + 2 \arctan(\delta\kappa/k_x) \quad (2.5)$$

where $\delta = n_a/n_b$ is the index ratio and only differs from Equation 2.4 with this parameter. conclusively, the less is δ parameter, the propagation constant of TE and TM modes are closer.

2.1.2 Dispersion relation

Based on Equation 2.4 and Equation 2.5, k_x can be solved and then utilized to calculate propagation constant β , since $n_a^2 k^2 = k_\perp^2 + \beta^2$. In the case of channel waveguides, the TE and TM solutions are both necessary. Therefore, propagation constants β can be expressed as the product of free space wave vector k and the

¹Since the planar waveguide is infinite at the y -direction, thus the solution is identical in arbitrary xz -plane, which means no gradient along x -axis.

effective index n_{eff}

$$\beta = n_{\text{eff}}k = n_{\text{eff}}(\lambda) \frac{2\pi}{\lambda} = n_{\text{eff}}(\omega) \frac{\omega}{c} \quad (2.6)$$

along with the differential form

$$\frac{d\beta}{dk} = n_{\text{eff}} + k \frac{dn_{\text{eff}}}{dk} = n_{\text{eff}} - \lambda \frac{dn_{\text{eff}}}{d\lambda} \equiv n_g \quad (2.7)$$

$$\frac{d\omega}{d\beta} = c \frac{dk}{d\beta} = \frac{c}{n_g} \equiv v_g \quad (2.8)$$

which defines the group index n_g and group velocity v_g .

This formula linking $\beta - k$ or $\beta - \omega$ is named as dispersion relation, which gives the physics that light with different color propagates at different *speed*. Furthermore, Equation 2.4 and Equation 2.5 also indicate that the dispersion relation intrinsically depends on waveguide geometry.

2.2 Ring resonators

The ring resonators comprise of a bus waveguide and a ring waveguide, are usually demonstrated as optical filters or modulators at a wide range of platforms. The working principle of ring resonator can be derived completely [14] as an analogue to Fabry-Pérot etalon, based on the coupling mode theory.

In the model illustrated in Figure 2.2, the self-coupling coefficient τ and the cross-coupling coefficient κ can be evaluated analytically or using numerical simulation. Assuming the coupling only occur at the very close area, τ, κ are the power splitting ratios of the coupler and satisfy $\tau^2 + \kappa^2 = 1$ if the coupling section is lossless. a is the single-pass amplitude transmission, including both propagation loss in the ring and loss in the couplers.

The transmission rate of a all-pass type ring cavity takes the form of

$$T = \frac{I_{\text{pass}}}{I_{\text{input}}} = \frac{a^2 - 2a\tau \cos \phi + \tau^2}{1 - 2a\cos \phi + a^2\tau^2} \quad (2.9)$$

where $\phi = \beta L$ is the phase shift in a single round trip.

2.2.1 Coupling condition

By plotting the function in Figure 2.3, we can see, the extinction ratio of absorption peak is defined by the self-coupling coefficient τ and the single-pass amplitude transmission a due to device geometric differences, like the gap between the bus waveguide and the ring cavity. Namely, a and τ both determine the coupling condition, which can be categorized in three cases

- **weak coupling** $a > \tau$. The loss inside the ring is larger than the power coupled from bus waveguides.
- **critical coupling** $a = \tau$. The loss and self-coupling are in balance. The optical power restored in the resonator achieve the minimum.
- **over coupling or strong coupling** $a < \tau$. The coupling is too strong for the light to dissipate in a single round trip.

Previous work [15] proposed a method to evaluate the coupling condition above using the experimentally measured device transmission. Considering the loss in the coupler, bent segment of ring and higher mode perturbation, usually the critical coupling varies from modes and the cross section of waveguides [16].

2.2.2 Spectrum characteristics

Meanwhile, the minimum of transmission rate T can be achieved periodically as $\phi = 2m\pi$, which defines the resonance of ring resonators. Therefore, the resonance condition is derived as

$$\beta L = 2m\pi \quad (2.10)$$

where m is the mode index. Specifically, the propagation constant β , shall be an integral times of a quasi wave vector $2\pi/L$. With this condition, the free spectral range (FSR) of wavelength and frequency are obtained

$$\Delta\lambda_{\text{FSR}} \approx \frac{\lambda_{\text{res}}^2}{n_g L} \quad (2.11)$$

$$\Delta\omega_{\text{FSR}} \approx \frac{2\pi c}{n_g L} \quad (2.12)$$

In both wavelength and frequency domain, FSR determines the spacing of neighboring resonant peak. This is a significant factor when the ring resonators are designed.

Furthermore, from Equation 2.9, the full width at half maximum (FWHM) of the resonance spectrum is derived as $\delta\lambda$

$$\delta\phi = \frac{2(1-a\tau)}{\sqrt{\tau a}} \quad (2.13)$$

Likely, since the phase ϕ is related with the wave vector k in Equation 2.7. Substituting $\delta\phi = Ln_g\delta k$, the half width of wavelength is

$$\delta\lambda = \frac{d\lambda}{dk}\delta k = \frac{\lambda_{\text{res}}^2}{2\pi Ln_g} \frac{2(1-a\tau)}{\sqrt{\tau a}} \quad (2.14)$$

the same, at the frequency domain

$$\delta\omega = \frac{d\omega}{dk}\delta k = \frac{c}{Ln_g} \frac{2(1-a\tau)}{\sqrt{\tau a}} \quad (2.15)$$

Note in Equation 2.11 Equation 2.12 Equation 2.14 and Equation 2.15, the group index n_g is explicit instead of the effective index n_{eff} because both free spectral range and full width depend on the differential form, Equation 2.7.

And the finesse F of the resonator is defined

$$F \equiv \frac{2\pi}{\delta\phi} = \frac{\pi\sqrt{\tau a}}{2(1-a\tau)} \quad (2.16)$$

Finally, we define the quality factor, a measure of the sharpness of the resonance relative to its central frequency.

$$Q = \frac{\lambda_{\text{res}}}{\delta\lambda} = \frac{\pi Ln_g\sqrt{\tau a}}{\lambda_{\text{res}}(1-a\tau)} \quad (2.17)$$

Usually, the Q -factor can be decomposed into two parts by formula $Q^{-1} = Q_i^{-1} + Q_l^{-1}$. And Q_i, Q_l are intrinsic Q -factor and loaded Q -factor, referring to the loss inside the ring waveguide and at the coupler, respectively. The physical meaning of the finesse and Q -factor relates to the number of round-trips before being lost to internal loss and the bus waveguides when the power is depleted to $1/e$ of its initial value.

2.3 Third-order nonlinear optics

Although the nonlinear effect is ignored during the derivation of waveguide modes in Section 2.1, for numerous materials, the nonlinear response of electric field is significant even at mW level, which is easy to occur with assistance of modern lasers. The origin of nonlinear optic phenomena is similar to the movement of the object in a potential field, such as the ball-spring model.

In the nonlinear material, the atoms or molecules are driven by the external electric field, due to the around chemical bonds or molecular orientation, the displacement of atoms or molecules perform nonlinear dependence on the strength of field. In real-world materials, interaction coming arising from various frequency leads to the addition or subtraction of these frequency components. This explains the frequency conversion nature in nonlinear optics.

It is worth mentioning that not only in the bulk crystals, but also in the sub-micron scale [17], the nonlinear response is still efficient, even over a single-layer two-dimensional material.

Here, a brief theoretical derivation is elucidated and in the following part, degenerate four wave mixing is emphasized. In an isotropic nonlinear medium, assuming only instantaneous dielectric response, the relation between the polarization and the electric field is expressed by a power series in the electric field

$$\begin{aligned}\mathbf{P}(t) &= \epsilon_0(\chi^{(1)}\mathbf{E}(t) + \chi^{(2)}\mathbf{E}^2(t) + \chi^{(3)}\mathbf{E}^3(t)) \\ &= \epsilon_0\chi^{(1)}\mathbf{E}(t) + \mathbf{P}_{NL}(t)\end{aligned}\quad (2.18)$$

Note in Equation 2.18, the nonlinear susceptibilities $\chi^{(2)}$ and $\chi^{(3)}$ are second-rank and third-rank tensors, corresponding to the tensor product with \mathbf{E}^2 and \mathbf{E}^3 . The higher order response is neglected and sequentially, only $\chi^{(2)}$ processes and $\chi^{(3)}$ processes are to be introduced.

$\chi^{(2)}$ processes

In centrosymmetric crystals such as silicon, the second-order susceptibility term is absent. However, in other materials like lithium niobate (LiNbO_3) and aluminum nitride (AlN), the second-order nonlinearity are essential to realize electro-optic modulation and second harmonic generation.

$\chi^{(3)}$ processes

Silicon and silicon nitride are both cubic crystal. Due to the third-order dependence, another factor equivalent to the optical intensity is involved, the $\chi^{(3)}$

process is also named as intensity-dependent effect or Kerr effect.

Consider three frequency components of \mathbf{E}^3 , using the complex expression of electric field

$$\mathbf{E}(\mathbf{r}, t) = \sum_{k=1}^3 \mathbf{E}_{\omega_k}(\mathbf{r}, t) = \frac{1}{2} \sum_{k=1}^3 (\mathbf{E}_{\omega_k}(\mathbf{r}) e^{i\omega_k t} + c.c.) \quad (2.19)$$

Substituting into third-order term in Equation 2.18 and arranging with the same propagation direction, the third-order polarization is

$$\mathbf{P}^{(3)}(t) = \frac{3}{4} \epsilon_0 \chi^{(3)} [|\mathbf{E}_{\omega_1}|^2 \mathbf{E}_{\omega_1} + \dots] \quad \text{SPM} \quad (2.20)$$

$$+ \frac{6}{4} \epsilon_0 \chi^{(3)} [(|\mathbf{E}_{\omega_2}|^2 + |\mathbf{E}_{\omega_3}|^2) \mathbf{E}_{\omega_1} + \dots] \quad \text{XPM} \quad (2.21)$$

$$+ \frac{1}{4} \epsilon_0 \chi^{(3)} [(\mathbf{E}_{\omega_1}^3 e^{i\omega_1 t} + c.c.) + \dots] \quad \text{THG} \quad (2.22)$$

$$+ \frac{3}{4} \epsilon_0 \chi^{(3)} \left[\frac{1}{2} (\mathbf{E}_{\omega_1}^2 \mathbf{E}_{\omega_2} e^{i(2\omega_1 + \omega_2)t} + c.c.) + \dots \right] \quad \text{FWM} \quad (2.23)$$

$$+ \frac{3}{4} \epsilon_0 \chi^{(3)} \left[\frac{1}{2} (\mathbf{E}_{\omega_1}^2 \mathbf{E}_{\omega_2}^* e^{i(2\omega_1 - \omega_2)t} + c.c.) + \dots \right] \quad \text{FWM} \quad (2.24)$$

$$+ \frac{6}{4} \epsilon_0 \chi^{(3)} \left[\frac{1}{2} (\mathbf{E}_{\omega_1} \mathbf{E}_{\omega_2} \mathbf{E}_{\omega_3} e^{i(\omega_1 + \omega_2 + \omega_3)t} + c.c.) + \dots \right] \quad \text{FWM} \quad (2.25)$$

$$+ \frac{6}{4} \epsilon_0 \chi^{(3)} \left[\frac{1}{2} (\mathbf{E}_{\omega_1} \mathbf{E}_{\omega_2} \mathbf{E}_{\omega_3}^* e^{i(\omega_1 + \omega_2 - \omega_3)t} + c.c.) + \dots \right] \quad \text{FWM} \quad (2.26)$$

In above equations, \dots stands for all possible permutation terms contributed by frequencies $\omega_1, \omega_2, \omega_3$. The abbreviation on the right side represent for

SPM, self-phase modulation

SPM adds an intensity-dependent term except the linear polarization, leading to a broadening of the pulse spectrum.

Note the $\chi^{(3)}$ is complex, thus the imaginary part may contribute to another intensity-dependent absorption mechanics, which is usually depicted in the two-photon absorption (TPA). The free carriers excited by TPA in further change the temporally both the absorption coefficient and the refractive index of material.

$$n = n_0 + n_2 I + i \frac{\lambda}{4\pi} (\alpha_0 + \alpha_2 I) \quad (2.27)$$

where the I is the intensity, n_2 is the Kerr coefficient and α_0, α_2 are related with TPA-induced free carrier absorption (FCA) and free carrier index (FCI) change, both interrelated with third-order susceptibility

$$n_2 = \frac{1}{cn_0^2\epsilon_0} \frac{3}{4} \operatorname{Re}\left\{\chi^{(3)}\right\} \quad (2.28)$$

$$\alpha_2 = \frac{-\omega}{c^2 n_0^2 \epsilon_0} \frac{3}{2} \operatorname{Im}\left\{\chi^{(3)}\right\} \quad (2.29)$$

A figure of merit (FOM) is often used to compare the magnitude of Kerr coefficient n_2 with the strength of the TPA coefficient α_2

$$\text{FOM} = \frac{1}{\lambda} \frac{n_2}{\alpha_2} \quad (2.30)$$

XPM, cross-phase modulation

XPM can be seen the first signal index influenced by a second signal. And the coefficient of XPM is twice as strong as the SPM coefficient.

THG, third-harmonic generation

Like SHG, THG generated a new frequency with is one-third of input frequency.

FWM, four wave mixing

In FWM process, more than three frequencies are involved. Nevertheless, Equation 2.23 and Equation 2.24 contain two identical wave, sometime called as degenerate four wave mixing (DFWM). And Equation 2.25 and Equation 2.26 is a truly four wave process. Similar to the relation between SPM and XPM, the non-degenerate FWM is naturally twice stronger.

Traditionally, following the terminology in laser field, in DFWM, the ω_1 square term Equation 2.24 is labeled as pump frequency, and another two frequencies are referred to signal and idler frequency.

Besides, the imaginary part of third-order susceptibility incorporate other four-wave absorption mechanics, such as stimulated Brillouin scatter (SBS) and stimulated Raman scattering (SRS), which originate from acoustic waves in crystals and vibrating molecules.

Finally, it worth mentioning that in all THG and FWM processes, different from SPM and XPM processes, phase matching condition is required due to the

complex exponential factors. In this case, the phase mismatch can change the polarization rapidly and leads to periodical variation in these parametric processes.

2.4 Phase matching condition in nonlinear ring resonators

According to the previous section, in a typical nonlinear optical waveguide or silica fibers, despite the stimulated Raman and Brillouin scattering, the frequency conversion processes involve not only the self-phase modulation of pump light and cross-phase modulation of signal and idler light, but also the phase mismatch in four wave mixing propagation factor. In this case, it is necessary to study the coupled nonlinear equations involving signal, idler and pump intensity [18].

Whereas in ring resonators, whose mode linewidth (pm) is much narrower than self-phase modulation frequency broadening, the frequency broadening in single mode is negligible. Thus the phase mismatch among cavity modes becomes the critical factor of the band of four wave mixing.

In a typical FWM process, both energy conservation and momentum conservation are required

$$\beta_i + \beta_s = 2\beta_p \quad (2.31)$$

$$\omega_i + \omega_s = 2\omega_p \quad (2.32)$$

where the subscripts s i p stand for signal, idler and pump light.

Meanwhile, the resonance condition Equation 2.10 leads to $\beta = m \frac{2\pi}{L}$. Thus, Equation 2.31 is equivalent to

$$m_i + m_s = 2m_p \quad (2.33)$$

We can see that the momentum conservation agrees with mode number conservation. That is to say, as pump light sets into resonant wavelengths, by choosing the equidistant modes relative to the pump mode, the momentum conservation can be naturally satisfied. This is the most significant difference of ring cavities from non-resonant devices.

Therefore, phase mismatch can be estimated only in the frequency domain. By expanding a resonant angular frequency into Taylor series at ω_0 to the propagation constant β , at the distance of μ times FSR,

$$\begin{aligned}
\omega_\mu &= \omega_0 + \sum_{j=1} \frac{d^j \omega}{d\beta^j} \frac{(\beta - \beta_0)^j}{j!} \\
&= \omega_0 + \sum_{j=1} \frac{d^j \omega}{d\beta^j} \left(\frac{2\pi}{L} \right)^j \frac{\mu^j}{j!} \\
&= \omega_0 + D_1 \mu + \frac{D_2}{2!} \mu^2 + \frac{D_3}{3!} \mu^3 + \dots
\end{aligned} \tag{2.34}$$

where $D_j \equiv (\frac{2\pi}{L})^j \frac{d^j \omega}{d\beta^j}$ are j -order mode number dispersion parameter, whose dimension are all T^{-1} and $\mu \in \mathbb{Z}$ is the relative mode number.

It is easy to know that $D_1/2\pi = v_g/L$ is the free spectral range in the frequency and indicates that the dispersion property is related with the difference of resonant frequencies.

Next, we introduce the integrated dispersion D_{int} [19] to analyze the phase mismatch

$$\begin{aligned}
D_{\text{int}}(\mu) &\equiv \omega_\mu - (\omega_0 + D_1 \mu) \\
&= \frac{D_2}{2!} \mu^2 + \frac{D_3}{3!} \mu^3 + \dots
\end{aligned} \tag{2.35}$$

In particular, D_{int} is the residual dispersion higher than second order. Approximately, if $D_3 \mu \ll D_2$, the second-order dispersion will dominate the integrated dispersion both at signal and idler mode.

Indeed, the mode number dispersion parameter is linked with the dispersion coefficients in frequency and wavelength domain, giving such a chain rule

$$D_2 = -\frac{L}{2\pi} D_1^3 \beta_2 = \frac{L}{2\pi} \frac{\lambda^2}{2\pi c} D_1^3 D_\lambda \tag{2.36}$$

where $\beta_2 = d^2 \beta / d\omega^2$ is group velocity dispersion (GVD) and $D_\lambda = -(\lambda/c) d^2 n / d\lambda^2$ is the dispersion parameter.

In this method, we can analyze the phase mismatch in FWM quantitatively

$$\begin{aligned}
\Delta\omega &\equiv \omega_s + \omega_i - 2\omega_p \\
&= D_{\text{int}}(\mu) + D_{\text{int}}(-\mu) \\
&= 2 \left(\frac{D_2 \mu^2}{2!} + \frac{D_4 \mu^4}{4!} + \frac{D_6 \mu^6}{6!} + \dots \right)
\end{aligned} \tag{2.37}$$

From the above derivation, the frequency mismatch $\Delta\omega$ only adds to the even terms of Taylor series in Equation 2.34. To conclude, a rough presupposition to increase the efficient phase matched band is achieving zero and flat dispersion around pump wavelengths.

As we can see, based on the above derivation, light propagation in a nonlinear ring resonator involves not only basic guided optics but also nonlinear optics theory. In conclusion, four wave mixing in a ring resonator can be summarized as the frequency conversion progress occurring due to both waveguide confinement and cavity resonance under the specific phase matching condition. And much more interestingly, thanks to resonance in ring cavities, the phase matching condition is satisfied efficiently in the wave vector domain. To achieve frequency matching, the design and dispersion engineering will be introduced in detail in next chapter.

Chapter 3

Device design and dispersion engineering of nonlinear ring cavities

Mentioned above, second-order mode dispersion D_2 is the key factor in phase matching condition. In this case, a typical approach to reduce the dispersion offset is balancing the intrinsic material dispersion and structure induced dispersion—waveguide dispersion. This method is usually named as dispersion compensation. Typically, it requires greater film thickness which complicates the fabrication process, such as thicker film deposition and high-selectivity etching. Besides, it is only suitable for simple rectangular channel waveguides.

Furthermore, in some structures including slot waveguides, the waveguide dispersion features flat curvature in a appropriate dimension, indicating that by optimizing the structure, the material dispersion can be not only compensated but also flattened in a wide range. Another example is mode crossing, the avoiding crossing of dispersion curve, leads to local dispersion inversion even in a thin thickness.

In this chapter, above methods are described sequentially for the specific silicon nitride ring resonators. Beside, to improve the coupling efficiency, design of mode size convertors at bus waveguide input/output ports is also introduced.

3.1 Dispersion compensation

Indicated in Equation 2.4, the dispersion of integrated devices is not only the intrinsic material property, but also depends on the waveguide dimension. Thus, the phase mismatch arises as a result of both material dispersion D_M and waveguide dispersion D_W , $D_\lambda = D_M + D_W$. Here, we choose the wavelength dispersion parameter D_λ since the wavelength domain is measurable.

Material dispersion

Usually, the Sellmeier equation is used to fit the refractive index for a particular transparent medium based on the Lorentz-Drude mode. Luke *et al.* reported the below measured refractive index of stoichiometric Si₃N₄ film [20]

$$n_{\text{Si}_3\text{N}_4}^2 = 1 + \frac{3.0249\lambda^2}{\lambda^2 - 135.3406^2} + \frac{40314\lambda^2}{\lambda^2 - 1239842^2} \quad (3.1)$$

This Sellmeier equation is valid over the wavelength range 310–5504 nm and plotted in Figure 3.1, along with the material dispersion parameter D_M , which is calculated at the precision of nm using the second-order finite difference of refractive index. In the optical communication C-band 1550 nm, $n=1.9963$ and $D_M = -6.57 \text{ ps/km}\cdot\text{nm}$, This suggests the material dispersion at this range is considerably small. To note, the above Sellmeier equation is valid only for dehydrogenated stoichiometric silicon nitride. In most cases of common film growing, deposition sources and methods influence the refractive index significantly.

Waveguide dispersion

To evaluate the waveguide dispersion parameter, the numerical simulation using commercial software Lumerical MODE is performed to solve the modes effective index and cross section dimension is swept in the case of channel waveguide. The selected mode is fundamental TE modes, and the bent radius is set as 200 μm .

Shown in Figure 3.2, the dimension dependence of waveguide dispersion features negative values in a small size, i.e. behaving normal dispersion at the second order. Nevertheless, as either thickness or width increases, D_W turns positive. This indicates that to achieve zero dispersion in phase match condition during four wave mixing, the normal material dispersion can be compensated with anomalous waveguide dispersion.

For example, at 1550 nm, in a 1.5- μm -wide and 0.8- μm -thick silicon nitride waveguide cladded by silica, whose refractive index is 1.48, the waveguide dis-

persion is 122.56 ps/km·nm. Substituting into the second-order dispersion chain rule in Equation 2.36, the second-order mode number dispersion parameter D_2 is about 3.07 MHz, indicating a successful dispersion compensation for silicon nitride film whose D_M smaller than -100 ps/km·nm.

As a result, a common method to realize material and waveguide dispersion compensation is to first measure the film refractive index, fit use Sellmeier equations and choose waveguide dimension by wavelength dispersion parameter D_λ .

3.2 Dispersion engineering using slot structure

The slot waveguide was firstly realized by Xu *et al.* experimentally [21]. The same group, Almeida *et al.* then discussed the light enhancement and confinement caused by large discontinuity of the electric field at high-index-contrast interfaces [22]. In the recent decade, it is fully studied that such a novel waveguide can be also used to design dispersion-flattened waveguide [23–26], including the both vertical or horizontal and single or multiple slots. It is also reported that a micro-ring resonators formed by a slot hybrid waveguide exhibits a flat and low anomalous dispersion [27].

In our research, the vertical slot is preferred due to the easy monolithic fabrication. For example, in a double vertical slot waveguide illustrated in Figure 3.3, two extra gaps are fully etched and then reburied with low-index medium instead. Except the waveguide width w and thickness t , two extra parameters are defined, the position factor pf , ratio of slot position to the waveguide width w , and the filling factor ff , ratio of slot width to the waveguide width w .

To classify the modes in this slot structure, the same mode solver mention in previous section is performed. In the result shown in Figure 3.4, in TM0 and TM1 modes, the light is confined strongly in the slots while the TE0 and TE1 is similar to the normal TE modes, where the discontinuity is obvious on the upper and lower interfaces.

Furthermore, by optimizing the position and filling factors, the near-zero and flattened dispersion can be obtained. Shown in Figure 3.5, sweeping of five sets of parameters stands out not only efficient dispersion inversion but also flattening over waveguide dispersion D_W .

3.3 Effects of mode crossing

In the conclusion of Section 3.1, only in the wider or thicker waveguides can the zero dispersion be compensated. However, despite the fabrication difficulty arising from thicker films, the waveguide of larger size also supports high order modes.

In this case, due to the perturbation of high order modes, the linear mode coupling occurs and influences the resonance spectrum. In the study of soliton generation, it is found that avoided mode crossings induced by linear mode coupling can prevent optical soliton formation when affecting resonator modes close to the pump laser frequency [28, 29]. On the other hand, by introducing artificial mode crossing, the anomalous group velocity can also be achieved [30]. Even though the phenomena mentioned in these works are classical, but in the term of phase matching condition, the insight is similar in quantum optics. In the following research, the mode crossings found in our devices not only change the spectrum transmission, but also leads to failure of evaluating the dispersion properties.

3.4 Edge coupling

Much of related works, such as photonic crystals or whispering gallery mode resonators, use prism coupling or tapered fiber coupling for tunability of coupling condition. In the case of integrated ring resonators, the bus waveguides are designed in several distances, usually varying from under coupling to over coupling. Thus, the light confined in the bus waveguide can be directly coupled inwards or outwards using appropriate optical fibers. In previous works [31], both grating coupling and edge coupling were adopted. However, considering the broadband frequency conversion motivation, the edge coupling is preferred for a comparatively broader 3dB bandwidth.

To achieve high coupling efficiency, inverted tapered couplers are used as mode convertor. The input and output ports of waveguide are both tapered from normal width $1.5 \mu\text{m}$ to a narrower end. By finite-difference time-domain (FDTD) methods, the mode field is swept with several taper end widths.

From the result shown in Figure 3.6(a), the mode fields expand horizontally as the taper end width increases proportionally. The largest mode size of $3.4 \mu\text{m} \times 3.4 \mu\text{m}$ is successfully demonstrated, but the enhancement is not significant compared with no tapered port in Figure 3.6(e). In result, a lensed fiber with spot diameter from $3.0 \mu\text{m}$ to $3.4 \mu\text{m}$ is recommended.

Chapter 4

Device fabrication of silicon nitride ring resonators

Different from fabrication of silicon photonic devices based silicon-on-insulator (SOI) wafers, which is CMOS-compatible and widely used in the laboratory and semiconductor industry, to fabricate integrated silicon nitride device, in particular high Q -factor ring resonators realizing four wave mixing, is still challenging. Collaborating with Yokoyama Lab in Kyushu University, we perform the subtractive fabrication of silicon nitride ring resonators as well as other optical devices.

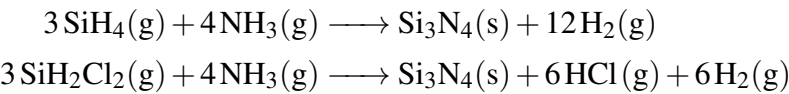
The subtractive process refers to the subtraction of unnecessary parts after the patterning, differing from the lift-off or damascene processes. For optical devices, it challenges the etching recipe to achieve less roughness on the sidewalls. The previous work using similar fabrication processes reported silicon nitride ring resonators with Q -factor up to 5.2×10^4 . The measured loss of waveguides is 2.9 dB/cm [32].

The schematic process flow of the subtractive process is illustrated in Figure 4.1. First, the silicon dioxide film is deposited on a 4-inch silicon substrate using the TEOS (tetraethyl orthosilicate) source. An alternative method is using a thermal oxidized silicon wafer directly. The target thickness of silicon dioxide layer is greater than 2 μm to create enough buffer between the silicon nitride film and the silicon substrate. Next is silicon nitride film deposition using chemical vapor deposition methods. Following electron beam (EB) lithography patterning, the silicon nitride layer is etched with inductively coupled plasma reactive-ion etching (ICP RIE) technique. After the resist removal, another layer of silica is cladded. Finally, the chip is cut to couple the light from the edge.

The details of each step will be expanded in the following contents.

4.1 Film deposition

Low pressure CVD (LP-CVD) is a traditional method to deposit silicon nitride from the vapor source by the decomposition of chemicals on the surface. Stoichiometric silicon nitride can be obtained by controlling and optimizing the ratio of silicon and nitrogen sources. The precursor of silicon is usually silane (SiH_4) or chloride silane gases, such as dichlorosilane (DCS, SiH_2Cl_2). And the ammonia gas (NH_3) plays the role of nitrogen source.



Considering the toxic gases used in LP-CVD, an alternative approach is to use modern plasma-enhanced CVD (PE-CVD) with liquid source, which has faster growing rate and lower reaction temperature.

To compare the CVD method dependence of film properties, especially the refractive index, in our research, three different CVD facilities—LP-CVD, PE-CVD and liquid source CVD (LS-CVD) are exploited with corresponding recipes.

Compared with commercial silicon nitride on insulator wafers deposited using LP-CVD, the details of PE-CVD and LS-CVD recipes are listed in Table 4.1. It is apparent from the data that LS-CVD has the fastest rate 23 nm/min, and lowest reaction temperature. In addition, during our experiments, although the flow rate of SN-2 source changes the film growing rate, it does not effect the film stoichiometry and optical properties. It is also worth to mention that all the wafer deposited with above three recipes shows no cracks during our fabrication, suggesting low tensile in these silicon nitride films.

4.2 Patterning

The sample used in our experiments are usually in the size of $20 \text{ mm} \times 20 \text{ mm}$, diced off from a 4-inch wafer. All the samples are cleaned several times using acetone solution in a ultrasonic cleaning device for at least 5 min. Before resist coating, a step of oxygen ashing is helpful to remove the particles over sample surface.

First, a layer of an adhesion promoter, hexamethyldisilazane (HMDS) is coated at 2000 rpm and then baked at 120°C for 1 min. Next, the positive resist (AR-P 6500, ALLRESIST GmbH) is coated at 1000 rpm and soft-baked at 120°C for 2

min. The final thickness of resist is around 800 nm to achieve enough thickness during the etching process. The main electron-beam lithography (EBL) machine used in our experiments is ELIONIX ELS-F100 and the beam dose is 3 nA, 0.6 sec/dot. This recipe is fully optimized and has small feature sizes and high accuracy around 10 nm. After the lithography, the sample is developed using *o*-xylene for 1 min.

4.3 ICP etching

In order to etch the waveguide layer selectively, ICP-RIE (RIE-400iPB, SAMCO Inc.) is used to remove the unmasked section in silicon nitride layer.

Different from previous work [15], the ICP-RIE facility used in this study is optimized for deep silicon etching. In the key etching step of our recipe, only CHF₃ gas, 6 sccm, is used as well as with argon gas to cleans any residual organic matter over the surface. ICP power is set 50 W, and RF bias power is 20 W.

The etching rate of three kinds of film is listed in Table 4.1. From the data, we can see LS-CVD deposited film has the best selectivity, much higher than LP- and PE-CVD samples. It seems possible that the film density varies from the CVD methods, due to LS-CVD has the fastest growth rate and lowest reaction temperature.

4.4 Top oxide cladding

The final step is cladding another layer of silicon dioxide to increase the coupling efficiency of ring resonators, as a result of lower index contrast. Before film deposition, to remove not only the residual EB resists but also the polymer generated during the plasma etching, all the samples are first deeply ashed using normal oxygen recipe in another RIE facility. To reduce the damage of waveguide sidewall, this step is cycled with organic cleaning. As same as the buried oxide layer, TEOS source is used to deposit another 2-3 μm top cladding layer with the same LS-CVD facility.

4.5 Annealing

To remove the residual hydrogen in silicon nitride film, an optional step of annealing is necessary. Traditionally, annealing process can be performed in different

cases, after or during CVD deposition [33], after dry etching or after top cladding [34]. Since the first case requires tensile control during cycled deposition-annealing operation [33], in our experiments, annealing before or after top cladding of negatively patterned LS-CVD and PE-CVD sample are merely compared.

To achieve high vacuum during the annealing, we use a tube-type electric furnace. In a high vacuum, the furnace is set first heating gradually from room temperature to 300 °C for 1 h, then heating to 1000 °C for 3 h, keeping at 1000 °C for 4 h, and cooling down to 300 °C for 5 h, then naturally cooling to room temperature.

Shown in Figure 4.2, there are cracks on both the LS-CVD and PE-CVD samples. In contrast, the negatively patterned samples are free of any cracks but is severely contaminated, which possibly results from the residua in the tube furnace. In general, the finding of cracks on the top clad layer shows despite the tensile control over the silicon nitride film, even negative EB resist is used for layout transfer, it is still difficult to annealing the typical TEOS cladded samples with the PE-CVD facility in our fabrication condition.

4.6 Chip dicing

The final step of fabrication is to disclose the input and output ports of bus waveguides. A conventional method is using diamond scribe to define the direction of wafer cleaving, whose accuracy depends on scribe end width. While in the case of devices with mode convertors, to precisely define the input and output ports, the chip dicing is required.

Compared with conventional mechanical dicing, the laser dicing technique is advantageous at high precision and less damages on the chip edges. The image of laser diced edge is compared with the manually diced one in Figure 4.3. Apparently, the chip using laser dicing has smoother edge, which is helpful to reduce the backward scattering during fiber launching.

4.7 Summary

To summarize the fabrication process used for silicon nitride ring cavities, several problems occur and result in device nonresonance sometimes. First is the cleaning, we found using organic solution is not enough for particle removal before spin coating. A solution can be multiple filtering of electron beam resist. Another problem is film etching. Previous research [35] studied different etching recipes, which are not covered in this thesis. But due to low recipe reproducibility, fully optimization is still necessary. Furthermore, the trade-off between film thickness and annealing still exists. An future alternative is using metallic hardmask against the etching plasma and adding deeper trenches around ring resonators to prevent cracking.

Chapter 5

Device evaluation and dispersion analysis of samples fabricated using various CVD methods

During and after the fabrication, the film property and devices are then fully estimated. To compare the chemical vapor deposition method differences, the material properties, especially the infrared band absorption is first studied. By using tunable laser based spectrum measurement, device optical transmission is then analyzed. Finally, this chapter is closed by the discussion of dispersion behavior shown in fabricated devices.

5.1 Material properties

5.1.1 Ellipsometry

Using the infrared ellipsometry, the refractive index of deposited silicon nitride film is obtained. The result is shown in Figure 5.2, where we can see the index varies from the deposition methods at the magnitude of 0.01. Furthermore, even the refractive index are distinguished, the material wavelength dispersion parameter D_M can be close.

5.1.2 Fourier-transform infrared spectroscopy

The vast majority of studies on silicon nitride fabrication processes have found that the hydrogen remaining in the films leads to N-H and Si-H bonds, which

causes the optical absorption at S and C band [36, 37]. To quantitatively clarify these bonds in our film, we perform the Fourier-transform infrared spectroscopy (FTIR) on the top of silicon nitride film.

The measurement is carried out using attenuated total reflection (ATR) method with SHIMADZU IRTtracer-100. In Figure 5.1, the absorbance is taken from the difference with background transmittance. It can be seen that except the peak around 780 cm^{-1} referring to Si-N stretching mode, two other peaks are located around 2150 cm^{-1} and 3350 cm^{-1} , corresponding to Si-H and N-H bonds respectively.

Interestingly, there are also two peaks found at 1020 cm^{-1} and 1120 cm^{-1} , indicating Si-O symmetric and asymmetric stretching modes in bottom silica. This result may be explained by the fact that in ATR method, the depth of penetration at this wavelength is less than 1 micron, while the thickness of silicon nitride layers in our experiment is targeted at 800 nm.

In conclusion, even though the ammonia free recipe is used in LS-CVD method, the film is still hydrogenated while LP-CVD commercial wafers show least N-H absorbance.

5.2 Device transmission

5.2.1 Methods

In the example given in Section 3.1, a typical dispersive ring resonator has the D_2 value around MHz, which means the given free spectra range (FSR), for example 100 GHz, is greater than the next one in a MHz-level difference. It is difficult to achieve such precise measurement using traditional optical spectrum analyzer whose typical resolution is around pm, 100 MHz. The tunable laser scanning is developed to solve this problem, especially assisted by an external frequency comb [38].

Here, we exploit the method using laser step triggering to calibrate the real-time measured device transmission. Compared with the frequency comb or wave meter assisted spectroscopy, this method is much more convenient to deploy. By increasing the data acquisition sampling rate or alternating with electric oscilloscope, the wavelength precision can be further improved. Given the well-resonant spectrum, the dispersion information is further extracted from the transmission, in particular the resonant peaks.

Fiber launching

Using two five-axis fiber alignment stages (Newport M-562F-XYZ & M-562F-XYZ-LH), the device ports are aligned with two lensed fibers on both sides. The spot size of lensed fibers is $2 \mu\text{m}$, see Figure 5.3(a) and (b), which is not optimized to the size mentioned in Section 3.4.

Before any following experiments, the output port is first coupled to the infrared InGaAs camera in free space using a $20\times$ objective lens. To align the chip input port precisely, the real-time images is used to adjust all the three degrees of freedom until the spot is observed explicitly on the screen, see Figure 5.3(c). Next, by carefully rotating the palettes of polarization controller on the input side, the device coupling can be built in either TE or TM mode. Then another lensed fiber is launched instead and aligned carefully, as the power meter reading is referred to.

In this method, the best facet-to-facet coupling efficiency is around 6 dB in the case of LIGENTEC samples introduced in Chapter 6, where is optimized by mode convertors. Comparatively, a more typical facet-to-facet loss without mode convertors can be 8-9 dB.

It is worth mentioning that all the chips are set over a chip carrier (SURUGA SEIKI F126) equipped with a thermoelectric cooler (TEC). This is essential for long-time thermal stability, see Figure 5.3(a). With TEC connected to an external temperature controller, the temperature precision around device under test can be 0.1°C . To avoid moisture condensation, the TEC is set a little higher than room temperature, 30°C in our case.

Spectrum sweeping

The schematic diagram of the device spectrum measurement is shown in Figure 5.4. After manual alignment, the tunable semiconductor laser (SANTEC TSL-710) is first set to continuously sweep from 1480 nm - 1640 nm, covering the optical communication S C and L bands. The internal power reference signal and the step trigger are also generated simultaneously, which are used to calibrate the output optical power and improve wavelength scanning accuracy. The output power from device under test is measured by the power meter (Newport 2963-R).

Compared with photon diodes, the power meter in our setup is critical to realize various range scanning. Finally, the signals of power reference, step trigger and device transmission are all synchronized with the data acquisition module, and then analyzed by the computer. To achieve pm-resolution spectra, transmitted

power is simply divided by power reference and the step trigger are marked to interpolate wavelengths in the certain time interval.

Peak searching

Given the transmission spectra, the negative peaks are located with peak-finding algorithm, yielding not only the peak location, but also the width and prominence. These values are next used to calculate the free spectral ranges and Q -factors. In general, due to the fabrication difference, not all the devices appear resonance in the measured band. To compensate the broken spectra, several algorithm are performed to achieve best performance of peak-finding.

In our technology, for the spectra with remarkable absorption illustrated in Figure 5.5, the background of raw spectrum is first calculated using digital filters. The filtered spectra are then used to search the peaks without the noise effects.

5.2.2 Thermal stability

Although silicon nitride is reported as high thermal conductivity material, the surrounding silicon dioxide is comparatively worse thermal conductive. Despite the room temperature fluctuation, the nonlinear phenomena usually requires high pump power intracavity, which heats the device significantly. In result, refractive index occurs and leads to resonance shift. Thus, the thermal sensitivity is a critical factor of nonlinear ring resonators.

For example, with the TEC set into different temperatures, the spectrum of same LP-CVD sample is then measured. Shown in Figure 5.6(a), temperature increasing leads to a obvious red-shift of the resonant peak. The wavelength range around 1630 nm is chosen for better transmission in this device. From Figure 5.6(b), the estimated thermal dependence of resonant wavelength $d\lambda/dT$ is $23 \text{ nm}/^\circ\text{C}$. In this case, if the Q -factor of ring resonator is up to 10^5 , even room temperature variation can results in totally off-resonance.

5.2.3 Results

To compare the material difference among the films deposited in three CVD methods, identical ring resonators layout is targeted to fabricate all these samples, film thickness is 800 nm, ring width is $1.5 \mu\text{m}$ and ring radius is $200 \mu\text{m}$. Since the thickness control during the film deposition and ICP etching is tough, all the devices are label with the waveguide height measured by step profiler before TEOS

top cladding. In particular, LP-CVD device is 802 nm-thick and LS-CVD device is 885 nm-thick.

However, the fabrication of stoichiometric silicon nitride using PE-CVD method is not successful, a sample deposited using same machine but with a silicon-rich recipe is reported instead.

The device transmission spectrum is first measured, shown in Figure 5.7(a). It can be seen that there is strong optical absorption from 1500 nm to 1540 nm in each device. Recording to the FTIR result shown in Figure 5.1, in particular LP-CVD sample containing almost no Si-H or N-H bonds, the optical absorption may originate from not only the residual hydrogen in silicon nitride but also top-cladding or bottom buried TEOS layer.

In addition, LP-CVD sample shows absorption at some certain wavelength, leading to the error values of peak finding. Such kind of broken spectra can be probably explained by the fabrication toleration, such like the gap is not fully etched or the ring resonator is contaminated. All these fabrication imperfection plays the role of scattering and also decreases the quality factors.

Furthermore, from the extracted resonant peaks, the Q -factors and frequency FSRs are summarized in Figure 5.7(b). The radius of each ring resonator are designed as 200 μm , corresponding to the FSR of 119.3 GHz. This agrees with the extracted FSRs of LP-CVD and LS-CVD devices. In the case of silicon-rich PE-CVD sample, the measured FSR of ring resonators near 1550 nm is around 94.3 GHz, indicating the refracting index of silicon-rich silicon nitride film is 0.34 higher.

In the term of Q -factors, counted in Figure 5.7(c), the LS-CVD samples have the highest quality factors whose mean value is 2.7×10^4 whereas the one of silicon-rich PE-CVD samples is 1.8×10^4 . The Q factor trend of LP-CVD device are similar to LS-CVD ones, but influenced by the broken resonance spectrum.

5.3 Dispersion analysis

Previous work [31] gave two methods analyzing the device dispersion, both depending on device transmission. One is to perform Fourier transform of the reflected spectra on the input port, which is equivalent to an etalon interference whose mirrors are waveguide input and output facets. Another method employs the cavity resonance instead. Despite the fabrication tolerance, considering the bent segment, the chromatic dispersion in the ring resonator is not identical to

the one in straight waveguides. Hence in our research, to the extract dispersion information accurately, the ring resonance method is preferred.

Following the integrated dispersion definition, the resonant wavelength λ_m is first converted to resonant frequencies ω_m . Before the polynomial fitting, the linear fitting is performed to evaluate first-order mode dispersion parameter. Then the integrated dispersion is calculated using the formula $D_{\text{int}}(\mu) = \omega_0 - D_1\mu$. The central frequency is ω_0 set as the center of scanning range. The relative mode numbers are constructed as a integer neighborhood of zero. A final step is the cubic or quadratic polynomial fitting. For a wider range scanning, a quartic curvature is more efficient, but in our case, the cubic polynomial is sufficient to extract second-order dispersion parameters in a 160 nm span.

For the samples fabricated using subtractive processes, due to the fabrication imperfection, not all the devices show efficient resonance, especially for LP-CVD and PE-CVD. The dispersion of devices fabricated above is only analyzed in the non-absorption range, 1550 - 1560 nm, shown in Figure 5.8. As we can see, in the case of LP-CVD and PE-CVD deposited films, thanks to the fine control of waevguide dimension, the dispersion are efficiently compensated. While due to different recipe used in PE-CVD one, non-stoichiometric silicon nitride stands out lagers material dispersion.

5.4 Summary

From the above result, the high Q -factor up to 5×10^4 is achieved using subtractive process though, in extensive experiments, no frequency conversion succeeded even with 100 mW level pump power. A possible explanation is that residual hydrogen in the CVD deposited films not only leads to near infrared range absorption, but also changes the effective nonlinear interaction of Si-N bonds. In this perspective, annealing processes is urgently demanded in our current fabrication flow.

Chapter 6

Fabless samples via foundries

Fabless photonic research is becoming a trend for its cheaper and easier external run [39]. There are several foundries all around the world offering the multi-project run service on integrated photonics and quantum optics applications, such as AMF in Singapore, LIGENTEC in Switzerland, LioniX in Netherlands and etc.

Except standard subtractive process used in previous chapter, to discover fabrication process diversity, we also design the device layout and order the devices fably. In the case of silicon nitride, two independent foundries are compared in the term of fabrication technique and device performance in the following sections.

6.1 Fabless process

The fabless sample involved in this research is ordered from LIGENTEC in Switzerland, and NTT-AT in Japan. Next, the process technique used is roughly introduced.

LIGENTEC technique

Photonic damascene process [40, 41] used in LIGENTEC samples improves the waveguide sidewall roughness by depositing the silicon nitride film into the etched thermal oxidized silica. By additive chemical mechanical planarization (CMP), the top surface of silicon nitride is polished.

The sample layout is illustrated in Figure 6.1. Five device groups with various FSRs are contained. In each specific group, the coupling gap is tuned from 400 nm to 700 nm in the step of 100 nm.

The microscope images of the sample is shown in Figure 6.2. Several layers of different structures are observed hierarchically, including the cross pattern stopping the crack during annealing and CMP, the waveguide layer and a top metallic layer for other users in the same run.

NTT-AT technique

NTT-AT technique adopts a different physical vapor method-reactive sputtering to deposit non-hydrogen silicon nitride. Compared with standard silicon sputtering, silicon atoms emitted from source react with the nitrogen gas flow into silicon nitride. Refractive index of the film deposited using this method is included in Figure 5.2.

In the term of design, the 4-inch wafer is customized with 22 cell in the layout shown in Figure 6.1, including the same design of LIGENTEC one in the special cell.

6.2 Device evaluation

6.2.1 Coupling evolution

Prior to cavity property evaluation, it is essential to compare the coupling condition among devices in the same group. Since the gap between bus waveguide and ring resonator is swept increasingly, usually the coupling condition turns from over coupling to critical coupling, and finally into weak coupling.

For the LIGENTEC Group 1, due to the reliable fabrication process, such an evolution of coupling condition is explicit. Presented in Figure 6.3(a), the coupling condition varies from over coupling to critical coupling, as the negative prominence of resonance peak increases. This tendency agrees with the Q -factor counts, shown in Figure 6.3(b). The other groups in the sample have similar feature but the critical coupling gaps are different.

6.2.2 Dispersion inversion

Thanks to the high quality fabrication of LIGENTEC damascene process, Group 1 and Group 2 show interesting dispersion inversion as ring widths increase. Presented in Figure 6.4, as the ring width is tuned from $0.8 \mu\text{m}$ to $1.7 \mu\text{m}$, the mode dispersion is inversed significantly, from -0.83 MHz to 1.46 MHz .

6.2.3 Comparison of quality factor and dispersion

Several works using the same LIGENTEC technique report ultrahigh Q -factors up to 3×10^6 [42, 43]. The same magnitude is also attained in Group 3 and Group 5. To compare the fabrication performance of both technique, two devices with the same design (Group 1 Device 4, gap 700nm, FSR 100 GHz, ring width 0.8 μm) are listed in Figure 6.5, as well as the Q -factor histograms.

For the transmission of LIGENTEC device in Figure 6.5(a) and NTT-AT device in Figure 6.5(b), there is no obvious absorption in the range 1500 nm - 1540 nm compared with the samples fabricated using non-annealing subtractive recipe. However, the quality factors of LIGENTEC devices are almost 4 times higher than NTT-AT ones. The histogram gathered in Figure 6.5(c) and Figure 6.5(d) features the same result.

We assume that despite the ammonia-free recipe used in NTT-AT technique, the etching recipe is not as fully optimized as LIGENTEC ones. It is also interesting to find that there is a clear difference of FSR trend. In particular, the increasing NTT-AT FSRs indicate a normal dispersion.

The identical devices mentioned above is further analyzed using the above method. The integrated dispersion is extracted in Figure 6.6. As we can see, the fabrication process influence the dispersion effectively as a result of different film growing method.

Chapter 7

Broadband photon pair generation

Back to the classical nonlinear optics theory, the solution to nonlinear coupling equations requires the initial power at either signal or idler mode, which is called seed light in the laser terminology. However, in quantum optics theory, all the cavity modes behave intrinsic vacuum fluctuation at a quantity of half $\hbar\omega$. Generally, even without light fed, the quantum fluctuation leads to photon emission at the single photon levels.

Once the single photon flux exceeds cavity threshold, the extracavity photon can be detected. To note, this kind of excitation is indistinguishable because the signal and idler photons are emitted simultaneously as a result of quantum mechanics, rather than signal photon stimulates idler photon and vice versa. In the language of quantum states, the state created intracavity contains both signal and idler photons. The wave packet is different from the normal single photon one. Further theoretical research [44] explained the squeezed nature of four wave mixing photon pairs, which is one of the exclusive properties of frequency entangled photon pairs.

In general, the photon pair or mode pair defined in our context refers to cavity modes are excited collectively under the phase matching condition. All the pairs are at a superposition of probability amplitude. Thus, under the weak coherent approximation, only two correlated photons exist in the wave packet, but the basis depends on allowed mode pair. Coincidence counting technology can be used to verify such correlation. As to generation band, it agrees with the classical phase matching condition.

7.1 Methods

Using the dispersion extraction method in Chapter 5, zero dispersion wavelength can be located easily among the measured band. In our experiments, optical communication band, especially C band is concentrated on, because enormous fiber optical components, like in-line filters are available in this range.

Illustrated in Figure 7.1, the setup of mode-resolvable singular photon pair generation first adopts a tunable laser as the pump source, whose display tunability is 0.1 pm and able to be tuned via external voltage input. The laser output is pumped into ring resonators using the fiber launching system.

A simple transmission scanning is then performed to select polarization mode. For high Q -factor devices, the transmission of TE and TM modes are separated in a distance of tens of pm. Thus, as either of the resonance vanished by rotating the polarization controller, the fiber launches the particular polarization mode in the bus waveguide. For low Q -factor cavities, since the TE and TM are degenerate in the spectrum, the method of polarization alignment is as same as the one using the InGaAs infrared camera.

Beyond the polarization selection, the pump wavelength should also be aligned to the cavity resonance. The on-resonance or off-resonance can be determined as the output power displays maximal distinction ratio. In our experiment, the pump peak around 1550 nm, usually presents at least 10 dB extinction before and after on-resonance.

Next, the output light are splitted 50% by 50% into signal and idler channels, indicating half of generated photons are lost. The two channels are sequentially filtered through two sets of band pass filters (Haphit Inc.). The pass band in the first set is 1540 ± 4 nm and 1560 ± 4 nm, respectively. The second set of band pass filters are tunable (WL Photonics Inc.) whose 3dB bandwidth is 0.12 nm. Since the free spectra range (FSR) in our device is much larger, the tunable band pass filter is adequate to select single mode at both channels.

Finally, each channel are detected by superconducting single photon detectors (SNSPD, SCONTEL) which are specific for infrared range. Since the SNSPD is polarization-sensitive, another two polarization controllers (not shown in Figure 7.1) are used to achieve maximal single photon counting during each measurement. At last, the time controller (ID Quantique, ID900) collects and records the counting time tag in the 100 ps resolution. Here, coincidence counting can be triggered directly or calculated later by data processing. The common coincidence window used in our experiments is 1 ns.

Coincidence counting

In quantum optics, coincidence counting is usually used to examine the non-locality of singular wave-particle. In our case, the photons which are splitted into two channels A and B yields the count per second (cps) N_A and N_B . Define the coincidence windows t , 1 ns commonly, and coincidence count (CC) is the number of two photon trigger events within this small time window, equivalent to the photon pair generation rate effectively. The accidental counting (ACC) is defined as $N_A N_B t$, alike to the background noise of counting system. Thus accidental-coincidence ratio (CAR) is defined as (CC-ACC)/ACC to reduce the noise effects.

It is worth to mention that in our research, the main topic is photon pair generation rather than photon state manipulation, in result numerous band-pass filters are exploited to realize mode-resolvable single photon counting. It does not contradict with distinguishability nature of frequency correlated photon pairs.

7.2 Low power photon pair generation

In this chapter, considering the mode spacing and Q -factors, LIGENTEC Group 2 Device 1 is mainly employed to perform photon generation, whose spectrum is presented in Figure 7.2. This device has FSR of 150 GHz and shows anomalous dispersion around 1550 nm given in Figure 6.4.

7.2.1 Single mode photon flux

With the pump power set as 100 μW and central wavelength at 1550.64 nm, the result of photon flux at both signal and idler bands versus relative relative mode index is presented in Figure 7.3. According to the 3dB bandwidth of band pass filters (BPF), the accessible relative mode index corresponds 7-14. To achieve higher photon counting, the central wavelength of tunable band pass filters (TBPF) is tuned carefully in the step of 0.01 nm.

In the result, there is trend that both signal and idler photon fluxes decreases as the mode index increases. It can be explained that phase mismatch of farther modes is greater than closer ones. The difference between signal and idler bands origins from the asymmetry of phase matching condition and filter spectral shape. As the input power is set as 100 μW , the estimated photon generation rate is around 10^3 cps/ μW per mode.

7.2.2 Coincidence counts of singular mode pair

In coincidence counts are measured in a 1ns coincidence window and in each mode, the time delay is set from -200 to 200 ps. The Figure 7.4 shows the result of coincidence counts and CAR. In the mode pair 9, single photon pair generation rate is 1500 per second, equals to 1.5×10^4 cps per mW, which is the highest rate observed at this input power level among all the samples.

As the mode number increases, coincidence counts varies roughly but in the CAR graph, such a trend is not obvious. This is due to the band pass filters used in our setup is not flat-top on the transmission spectrum. In conclusion, even several frequency-dependent optical components used in our setup, by calculating the coincidence-accidental ratio, the photon pair generation can be evaluated successfully.

7.3 Pump power dependence

Since spontaneous four wave mixing originates from Kerr nonlinearity, in classical nonlinear optics, converted power is linearly dependent on pump power. To confirm this relation in quantum scale, it is necessary to study both power dependence of photon flux and coincidence counts.

To amplify the pump power, a erbium-doped fiber amplifier (EDFA) is cascaded after the tunable laser. By increasing the output power, the power intracavity can exceed 500 mW. The mode passed through is fixed at $\mu = 9$, corresponding to $\lambda_i = 1540.28$ nm and $\lambda_s = 1558.79$ nm. During each cavity resonance alignment, the extinction ratio is kept around 10 dB. The result of photo flux is given in Figure 7.5. It is apparent that there is a continual growth of photon flux in both signal and idler modes.

Furthermore, the coincidence counting result is shown in Figure 7.6(a) where both maximal coincidence counts and background accidental coincidence counts increase with the pump power. While from CAR provided in Figure 7.6(b), higher input power leads to a significant decline. This can explained by the background noise arising from the Raman effect in optical fibers [11, 12]. As the nonlinearity of optical fibers is much weaker than silicon nitride device, in the high input power regime, it becomes obvious and contributes to the single photon count and decreases the coincidence count rate.

7.4 Joint spectral intensity

Since the spontaneous four wave mixing occurs simultaneously at each mode pair, the state generated in a broadband is equivalent to the intensity superposition all over the signal and idler bands. To clarify the quantum state characteristics in this view, usually the joint spectral filed or intensity is estimated to evaluate the frequency correlation [45, 46]. For example, compared with the N mode correlation measurement mentioned above, the two-party joint spectral intensity requires the coincidence measurement on the element in the whole N^2 hilbert space.

On the other hand, much of recent research concerning soliton generation discussed the thermal instability in the nonlinear ring resonators [47, 48]. To realize long time stable measurement, an auxiliary photon diode is added to monitor off-resonance situation illustrated in Figure 7.7. Using digital proportional–integral–derivative (PID) controller, which is deployed by a LabVIEW program, the tunable laser wavelength is tuned dynamically by the external voltage input. In this way, the extinction ratio of on-resonance is kept at a stable level as soon as possible. In addition, to increase the accessible mode number, the first set of BPFs in Figure 7.1 is replaced by a notch filter (OE Land Inc.). The pump power used here is 24.5 mW. This work is assisted by Kenta Sugiura.

During our measurement, the coincidence count is first scanned along the diagonal term of joint spectral intensity map to locate the central wavelength of tunable band pass filters when photon flux in Figure 7.8 is measured. In Figure 7.9(a), CC characterizes the peak at mode 13. This agrees with the result of photon flux. More obviously, both photon flux and CC suffer from the notch filter, whose 3dB cut bandwidth is larger the single FSR and not symmetric at signal and idler bands. After the diagonal scanning, the off-diagonal terms are then selected mode-by-mode. The grid-like distribution in ACC map, Figure 7.9(b) indicates the variation of measurement. As a result, the CAR presented in Figure 7.9(c) stands out no obvious off-diagonal fluctuation and features the frequency correlation in 46 mode pairs, corresponding a 106 nm (1499 nm - 1605 nm) span.

In this chapter, the frequency entangled photon pair is successfully generated using a high Q -factor anomalous dispersive silicon nitride ring cavity. The power dependence is studied and the mode-resolvable setup is performed thus a maximal 46 pairs of entangled photons is observed spontaneously, at 24.5 mW pump power.

Chapter 8

Summary

In above research, the silicon nitride ring cavities are fully studied as a source of frequency entangled photons.

To summarize up, in Chapter 3, dispersion compensation method for silicon nitride ring resonators was established thus gave the dimension requirement on waveguide cross section. In our conclusion, a 1.5 μm wide and 0.8 μm thick waveguide is suitable for zero dispersion at 1550 nm. Following this dimension, subtractive fabrication process were performed especially with films deposited using different CVD methods in Chapter 4.

In Chapter 5, the material properties of films used above is first studied using ellipsometry and Fourier-transform infrared spectroscopy (FTIR). Then all the fabricated device were estimated and compared in the term of Q -factors, FSR and mode dispersion. Transmission spectra of these devices show absorption around 1530 nm, which agree with the result of absorbance from FTIR. The highest Q -factor is up to 5×10^4 observed in samples using liquid source CVD. In the dispersion evaluation, our samples show highly agreement between the designed mode dispersion and measured values. In our future fabrication, such design is promising to realize broadband frequency entangled photon pair generation.

Furthermore, the fabless samples were introduced in Chapter 6 and featured high Q -factor up to 10^6 . Thus, we focused on the research of photon pair generation using Group 2 Device 1 in Chapter 7. The single photon flux is around 10^6 cps/mW and coincidence count is 10^4 cps/mW based on our measurement setup. By evaluating joint spectral intensity, 46 mode pairs show frequency correlation using 24.5 mW pump power.

In general, silicon nitride ring cavities behave outstanding performance as the source of frequency entangled photon pairs. Such devices also prove useful in expanding our understanding of how dispersion effect the pair generated in the term of broadband.

Here, we hope to give some future perspective on this topic.

First is on the device fabrication. Relative research like Kerr frequency combs offered some important insights of fabrication skills concerning dry etching and film tensile control.

Second, theoretically, the dispersion of ring cavities can be optimized into fully zero and flat from visible and infrared range, using computational iteration. But the photonic crystal could also be a powerful approach since the photonic band structure is able to confine the dispersion more efficiently referring to the research on slow-light generation.

Finally, in the field of optical quantum information processing, adding active devices such as electro-optic modulators can lead to manipulable frequency entanglement, which paves the way for future frequency-encoded optical quantum information technology.

Acknowledgements

First of all, I would like to thank my supervisor, Prof. Shigeki Takeuchi, without his continuing active support and knowledge I would not have made it this far. I would additionally also like to thank Associate Prof. Ryo Okamoto for discussions and lab support and Assistant Prof. Hideaki Takashima for discussions and teaching of the relevant topics.

I would also like to thank and acknowledge Xiaoyang Cheng, Jianxun Hong, Prof. Shiyoshi Yokoyama and the rest of the members at Kyushu University for our collaboration. I appreciate very much the great support and kindness I received when I visited. Most of the experimental results in this thesis have been possible thanks to you!

Moreover I would like to thank all the members of the Applied Quantum Electronics laboratory here at Kyoto University. I would like to thank Bo Cao for discussion on nonlinear optics and quantum optics, Toshiyuki Tashima for experience concerning FDTD simulation and Yu Mukai for discussion on FTIR. Specifically I would like to thank Kenta Sugiura for being great office mates providing discussions both around and beyond the topics that we are each working on, and other senior members for discussions on research topics. I would like to thank Masaya Arahat, Kazuki Fukushige, Issei Matsumoto and Masato Yoshikawa during our whole education and out-office experience. I would also like to thank other members for their discussion and office support on other research topics.

Additionally, I would like to thank the staff in Kyoto University Nanotechnology Hub for their technical support on device fabrication. I am grateful to other technicians providing instrumental support for our experiments.

Last, but not least, I would like to thank all of my family and friends home and abroad for being supportive and great to be around.

References

1. Wengerowsky, S., Joshi, S. K., Steinlechner, F., Hübel, H. & Ursin, R. An entanglement-based wavelength-multiplexed quantum communication network. *Nature* **564** (2018) 225–228.
2. Tchebotareva, A. *et al.* Entanglement between a Diamond Spin Qubit and a Photonic Time-Bin Qubit at Telecom Wavelength. *Phys. Rev. Lett.* **123** (2019) 063601.
3. Reimer, C. *et al.* High-dimensional one-way quantum processing implemented on d-level cluster states. *Nat. Phys.* **15** (2019) 148–153.
4. Okano, M. *et al.* 0.54 um Resolution Two-Photon Interference With Dispersion Cancellation for Quantum Optical Coherence Tomography. *Sci. Rep.* **5** (2015) 1–8.
5. Politi, A., Cryan, M. J., Rarity, J. G., Yu, S. & O’Brien, J. L. Silica-on-silicon waveguide quantum circuits. *Science* **320** (2008) 646–649.
6. O’Brien, J. L., Furusawa, A. & Vučković, J. Photonic quantum technologies. *Nat. Photonics* **3** (2009) 687–695.
7. Bonneau, D., Silverstone, J. W. & Thompson, M. G. Silicon quantum photonics. *Top. Appl. Phys.* **122** (2016) 41–82.
8. Kues, M. *et al.* On-chip generation of high-dimensional entangled quantum states and their coherent control. *Nature* **546** (2017) 622–626.
9. Paesani, S. *et al.* Generation and sampling of quantum states of light in a silicon chip. *Nat. Phys.* **15** (2019) 925–929.
10. Zhang, M., Feng, L.-T., Zhou, Z.-Y., Dai, D.-X. & Ren, X.-F. *Generation of multiphoton entangled quantum states in a single silicon nanowire* in *Adv. Photonics 2018 (BGPP, IPR, NP, NOMA, Sensors, Networks, SPPCom, SOF)* (OSA, Washington, D.C., 2018), IM3B.3.

11. Sugiura, K. *et al.* An on-chip photon-pair source with negligible two-photon absorption. *Appl. Phys. Express* **12** (2019)
12. Engin, E. *et al.* Photon pair generation in a silicon micro-ring resonator with reverse bias enhancement. *Opt. Express* **21** (2013) 27826.
13. Lu, X., Jiang, W. C., Zhang, J. & Lin, Q. Biphoton Statistics of Quantum Light Generated on a Silicon Chip. *ACS Photonics* **3** (2016) 1626–1636.
14. Bogaerts, W. *et al.* Silicon microring resonators. *Laser Photonics Rev.* **6** (2012) 47–73.
15. Ono, Y. *A study of photon-pair generation using silicon nitride ring resonators* Master Thesis (Kyoto University, 2017).
16. Pfeiffer, M. H., Liu, J., Geiselmann, M. & Kippenberg, T. J. Coupling Ideality of Integrated Planar High- Q Microresonators. *Phys. Rev. Appl.* **7** (2017) 1–8.
17. Leuthold, J., Koos, C. & Freude, W. Nonlinear silicon photonics. *Nat. Photonics* **4** (2010) 535–544.
18. Agrawal, G. in *Nonlinear Fiber Optics (Fifth Edition)* (ed Agrawal, G.) Fifth Edition, 397–456 (Academic Press, Boston, 2013).
19. Brasch, V. *et al.* Photonic chip-based optical frequency comb using soliton Cherenkov radiation. *Science* **351** (2016) 357–360.
20. Luke, K., Okawachi, Y., Lamont, M. R. E., Gaeta, A. L. & Lipson, M. Broadband mid-infrared frequency comb generation in a Si₃N₄ microresonator. *Opt. Lett.* **40** (2015) 4823.
21. Xu, Q., Almeida, V. R., Panepucci, R. R. & Lipson, M. Experimental demonstration of guiding and confining light in nanometer-size low-refractive-index material. *Opt. Lett.* **29** (2004) 1626.
22. Almeida, V. R., Xu, Q., Barrios, C. A. & Lipson, M. Guiding and confining light in void nanostructure. *Opt. Lett.* **29** (2004) 1209.
23. Mas, S., Caraquitena, J., Galán, J. V., Sanchis, P. & Martí, J. Tailoring the dispersion behavior of silicon nanophotonic slot waveguides. *Opt. Express* **18** (2010) 20839.
24. Zhang, L., Yue, Y., Beausoleil, R. G. & Willner, A. E. Flattened dispersion in silicon slot waveguides. *Opt. Express* **18** (2010) 20529.

25. Zhu, M. *et al.* Ultrabroadband flat dispersion tailoring of dual-slot silicon waveguides. *Opt. Express* **20** (2012) 15899.
26. Nolte, P. W., Bohley, C. & Schilling, J. Tuning of zero group velocity dispersion in infiltrated vertical silicon slot waveguides. *Opt. Express* **21** (2013) 1741.
27. Zhang, L. *et al.* Generation of two-cycle pulses and octave-spanning frequency combs in a dispersion-flattened micro-resonator. *Opt. Lett.* **38** (2013) 5122.
28. Herr, T. *et al.* Mode spectrum and temporal soliton formation in optical microresonators. *Phys. Rev. Lett.* **113** (2014) 1–6.
29. Bao, C. *et al.* Deterministic single soliton generation via mode-interaction in microresonators. *Opt. InfoBase Conf. Pap. Part F94-C* (2018) SW4M.2.
30. Kim, S. *et al.* Dispersion engineering and frequency comb generation in thin silicon nitride concentric microresonators. *Nat. Commun.* **8** (2017)
31. Sunada, Y. *Measurement of Group Velocity Dispersion of Silicon Nitride Ring Resonators toward Photon-pair Generation* Bachelor Thesis (Kyoto University, 2018).
32. Cheng, X., Hong, J., Spring, A. M. & Yokoyama, S. Fabrication of a high-Q factor ring resonator using LSCVD deposited Si₃N₄ film. *Opt. Mater. Express* **7** (2017) 2182.
33. Luke, K., Dutt, A., Poitras, C. B. & Lipson, M. Overcoming Si₃N₄ film stress limitations for high quality factor ring resonators. *Opt. Express* **21** (Sept. 2013) 22829.
34. Wang, L. *et al.* Nonlinear silicon nitride waveguides based on PECVD deposition platform. *Opt. Express* **26** (2018) 9645.
35. Ono, T., Okamoto, R., Tanida, M., Hofmann, H. F. & Takeuchi, S. Implementation of a quantum controlled-SWAP gate with photonic circuits. *Sci. Rep.* **7** (2017) 45353.
36. Ay, F. & Aydinli, A. Comparative investigation of hydrogen bonding in silicon based PECVD grown dielectrics for optical waveguides. *Opt. Mater. (Amst.)* **26** (2004) 33–46.
37. Agnihotri, O. P. *et al.* Advances in low temperature processing of silicon nitride based dielectrics and their applications in surface passivation and integrated optical devices. *Semicond. Sci. Technol.* **15** (2000)

38. Liu, J. *et al.* Frequency-comb-assisted broadband precision spectroscopy with cascaded diode lasers. *Opt. Lett.* **41** (2016) 3134.
39. Hochberg, M. & Baehr-Jones, T. Towards fabless silicon photonics. *Nat. Photonics* **4** (2010) 492–494.
40. Pfeiffer, M. H. P. *et al.* Photonic Damascene process for integrated high-Q microresonator based nonlinear photonics. *Optica* **3** (2016) 20.
41. Pfeiffer, M. H. P. *et al.* Photonic damascene process for low-loss, high-confinement silicon nitride waveguides. *IEEE J. Sel. Top. Quantum Electron.* **24** (2018) 1–11.
42. Yu, S. P. *et al.* Tuning Kerr-Soliton Frequency Combs to Atomic Resonances. *Phys. Rev. Appl.* **11** (2019) 1.
43. Vaidya, V. D. *et al.* Broadband quadrature-squeezed vacuum and nonclassical photon number correlations from a nanophotonic device (Apr. 2019) 1–10.
44. Scully, M. O. & Zubairy, M. S. *Quantum Optics* (Cambridge University Press, Sept. 1997).
45. Vernon, Z. & Sipe, J. E. Spontaneous four-wave mixing in lossy microring resonators. *Phys. Rev. A - At. Mol. Opt. Phys.* **91** (May 2015) 3006.
46. Vernon, Z. & Sipe, J. E. Strongly driven nonlinear quantum optics in microring resonators. *Phys. Rev. A - At. Mol. Opt. Phys.* **92** (2015) 1–17.
47. Guo, H. *et al.* Universal dynamics and deterministic switching of dissipative Kerr solitons in optical microresonators. *Nat. Phys.* **13** (2017) 94–102.
48. Herr, T. *et al.* Universal formation dynamics and noise of Kerr-frequency combs in microresonators. *Nat. Photonics* **6** (2012) 480–487.
49. Sinclair, G. F., Tyler, N. A., Sahin, D., Barreto, J. & Thompson, M. G. Temperature Dependence of the Kerr Nonlinearity and Two-Photon Absorption in a Silicon Waveguide at $1.55 \mu\text{m}$. *Phys. Rev. Appl.* **11** (2019) 1.

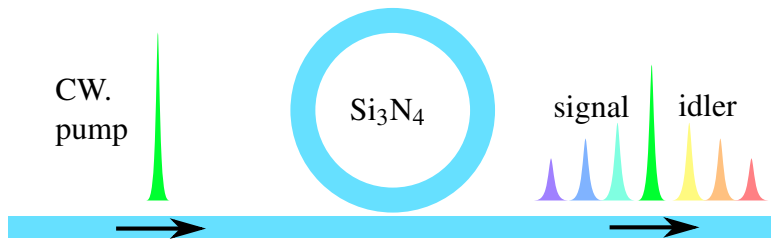


Figure 1.1: **Illustration of spontaneous four wave mixing in a silicon nitride ring resonator.** By pumping continuous wave laser, nonlinear Si_3N_4 ring cavities feature comb-like output.

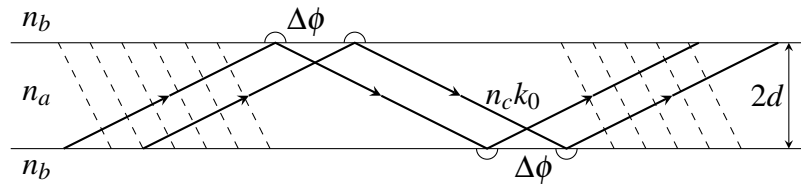


Figure 2.1: **Planar waveguide.** The upper and bottom layer are cladding and the middle is core layer. $\Delta\phi$ represents the Goos-Hänchen shift at the boundary.

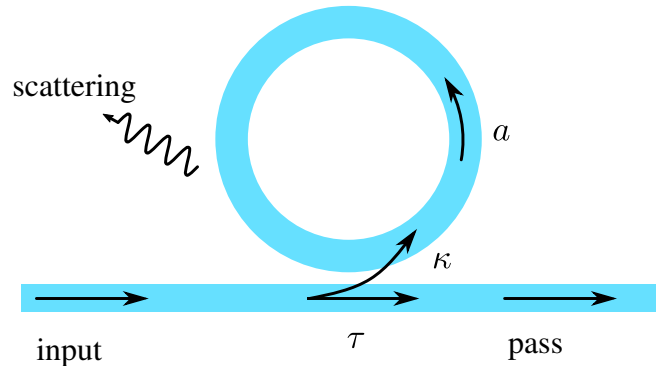


Figure 2.2: **An all-pass type ring resonator.** The transmitted spectrum is filtered periodically by the ring waveguide, in the case satisfying resonance condition. τ is the self-coupling coefficient and κ is the cross-coupling coefficient. a is the single-pass amplitude transmission including cavity scattering loss.

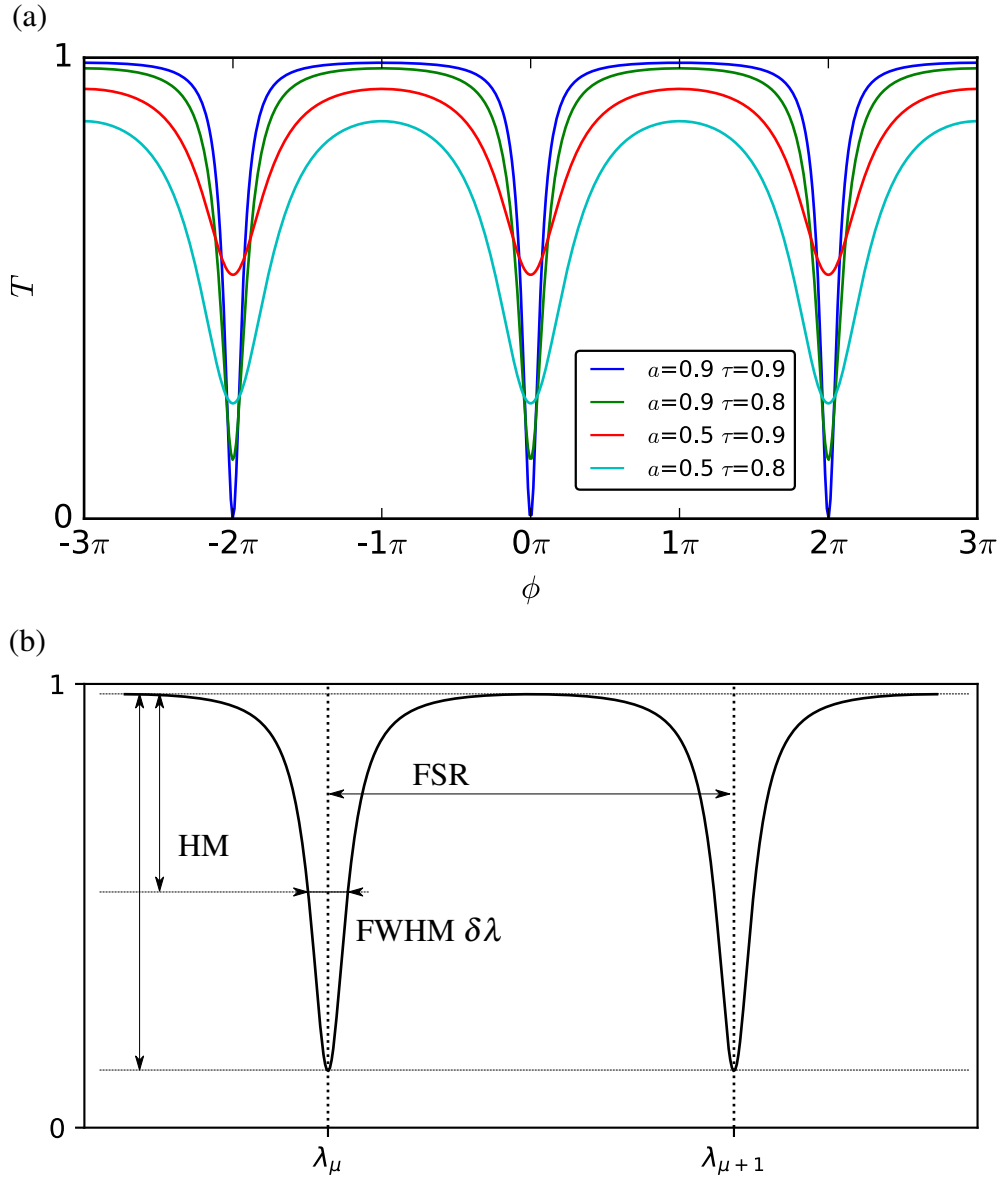


Figure 2.3: **Illustration of wavelength transmission spectrum of ring resonators.** **a.** Transmission spectrum is determined by coupling condition. Only when $a = \tau$ is critical coupling achieved. **b.** FSR, free spectral range, the distance between neighboring resonant wavelengths. FWHM, full width at half maximum.

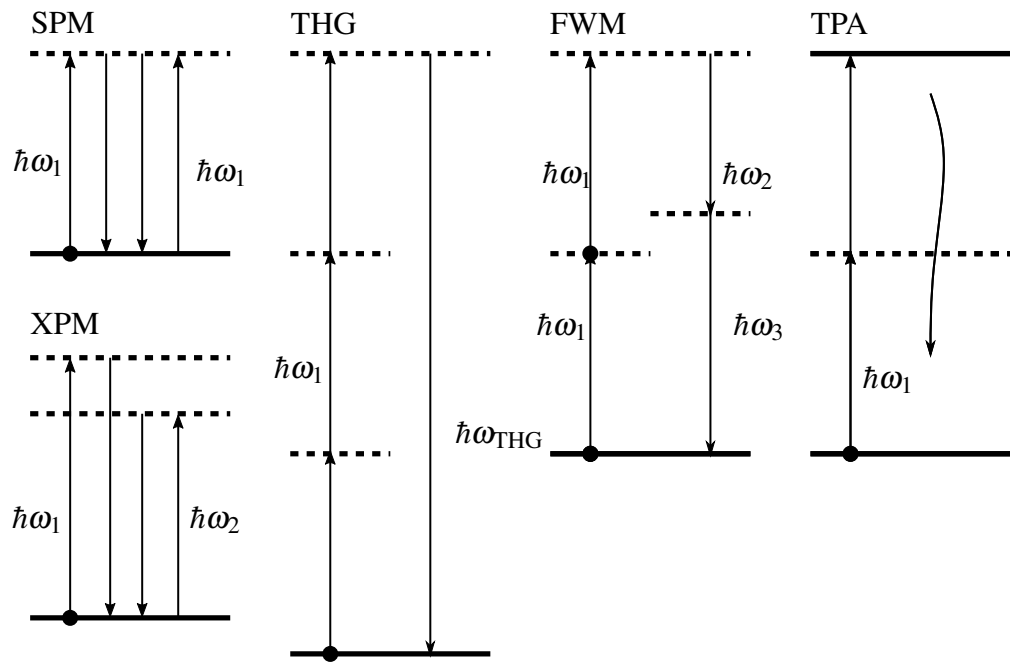


Figure 2.4: **Illustration of possible energy diagram in typical third-order non-linear processes.** SPM, self-phase modulation. XPM, cross-phase modulation. THG, third harmonic generation. FWM, four wave mixing. TPA, two photon absorption.

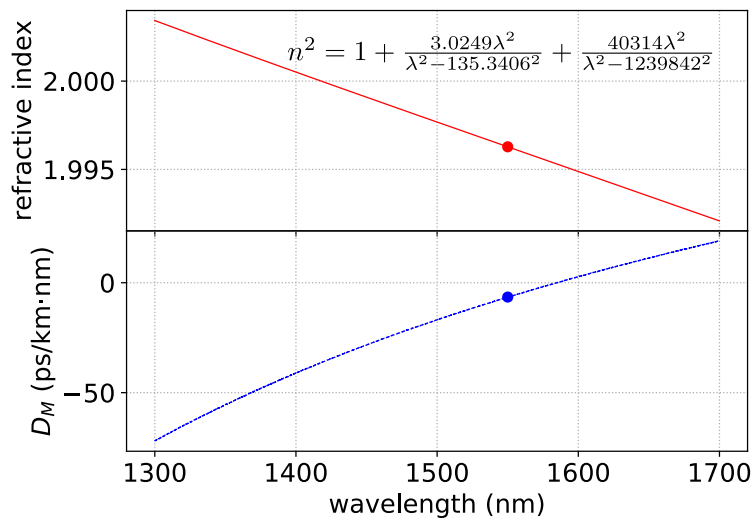


Figure 3.1: **Refractive index measured and material dispersion parameter from Reference [33].** As $\lambda=1550$ nm, $n=1.9963$ and $D_M = -6.5656$ ps/km·nm.

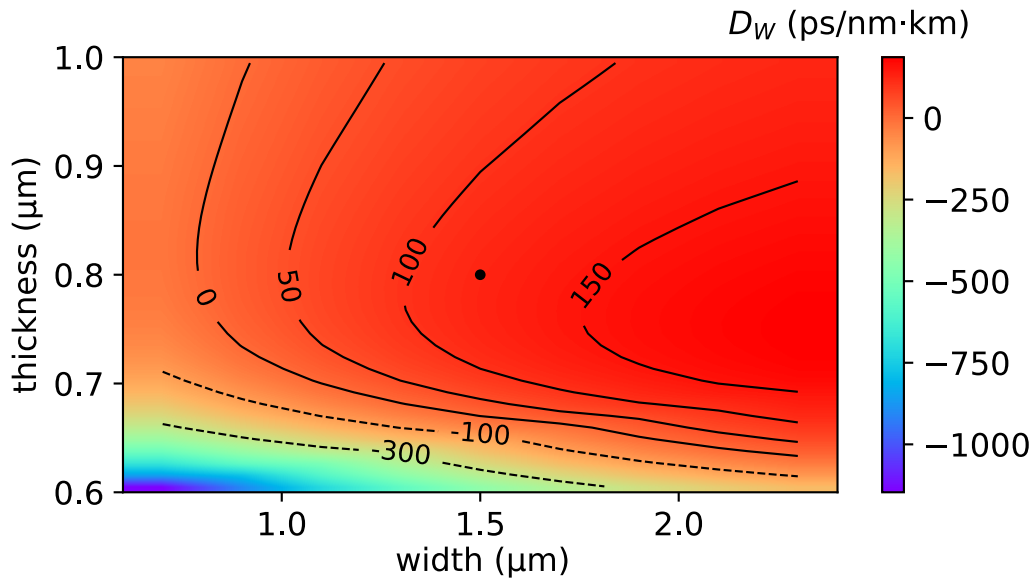


Figure 3.2: **Dimension dependence of waveguide dispersion simulated by Lumerical MODE.** The central wavelength to perform the simulation is 1550 nm. We select the fundamental TE mode to study the waveguide dispersion. The scattered point in the figure is 1.5- μm -wide and 0.8- μm -thick.

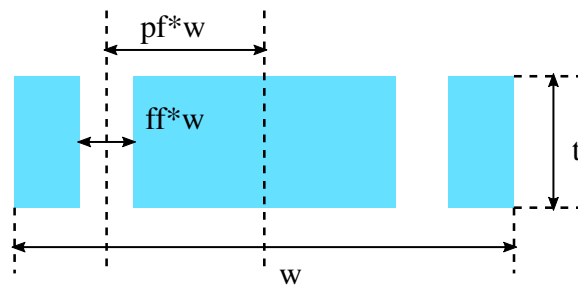


Figure 3.3: **Illustration of a double vertical slot waveguide.** The cyan region is Si_3N_4 waveguide and surrounded by silica.

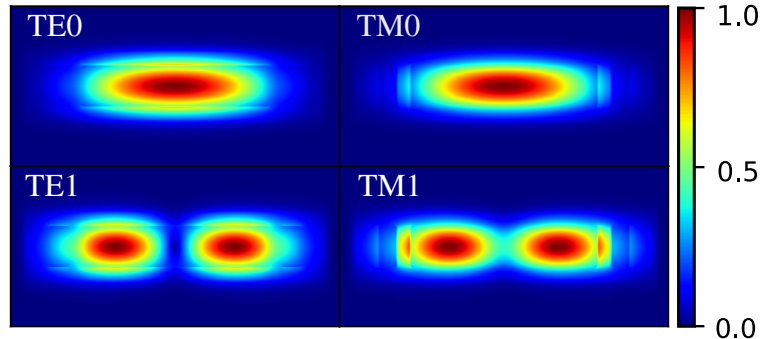


Figure 3.4: **Modes of the double vertical slot waveguide.** Calculated under $w=2.5 \mu\text{m}$, $t=0.8$, $ff=0.053 \mu\text{m}$, $pf=0.4 \mu\text{m}$

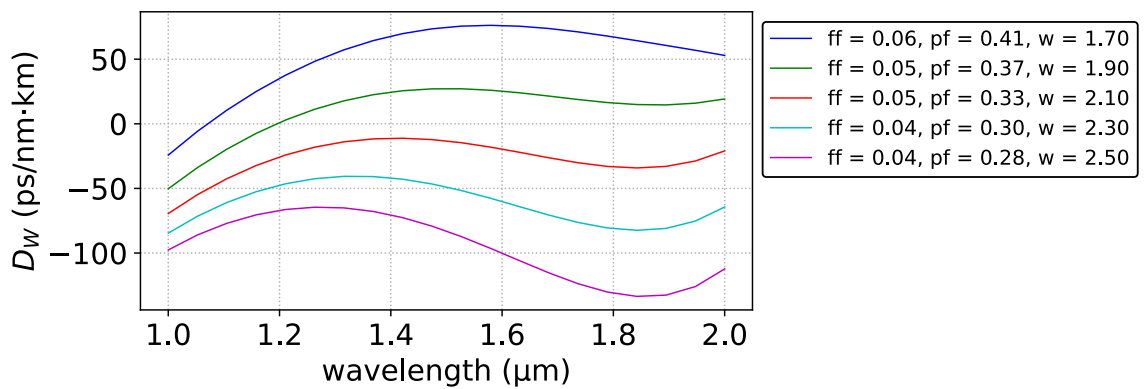


Figure 3.5: **Parameter sweeping for dispersion flattening using slot structure.** The waveguide thickness is fixed as $t=0.8$. Sweeping of five sets of parameters stands out not only efficient dispersion inversion but also flattening over waveguide dispersion D_W

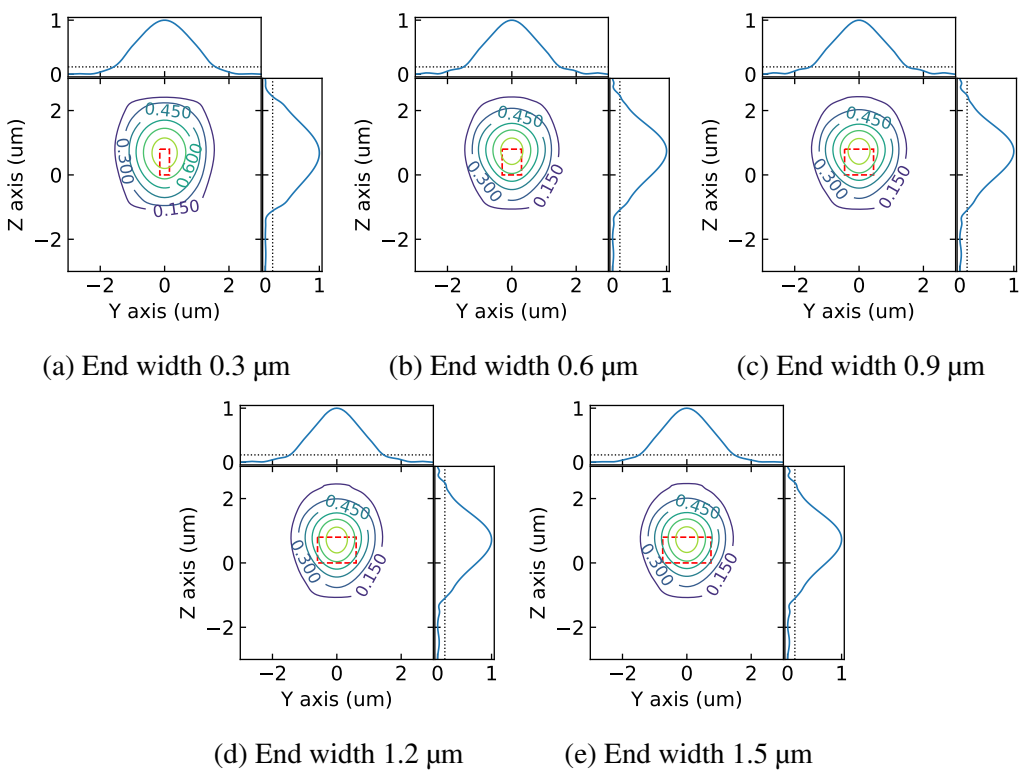


Figure 3.6: Mode field at the taper end by Lumerical FDTD. The film thickness is fixed as 0.8 μm and the taper edge is profiled in red dashed line.

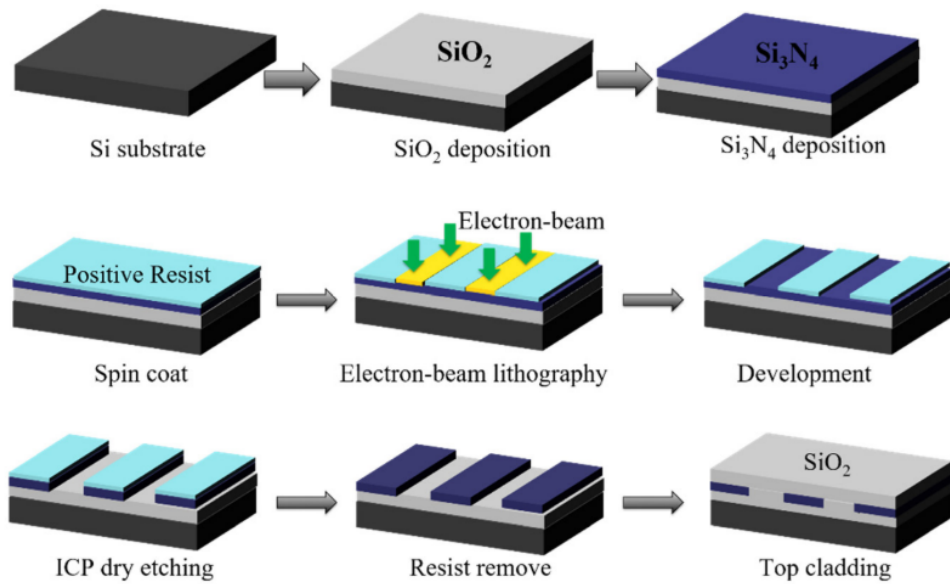


Figure 4.1: **Schematic process flow of the subtractive process from Reference [32].** The process used in this thesis is identical.

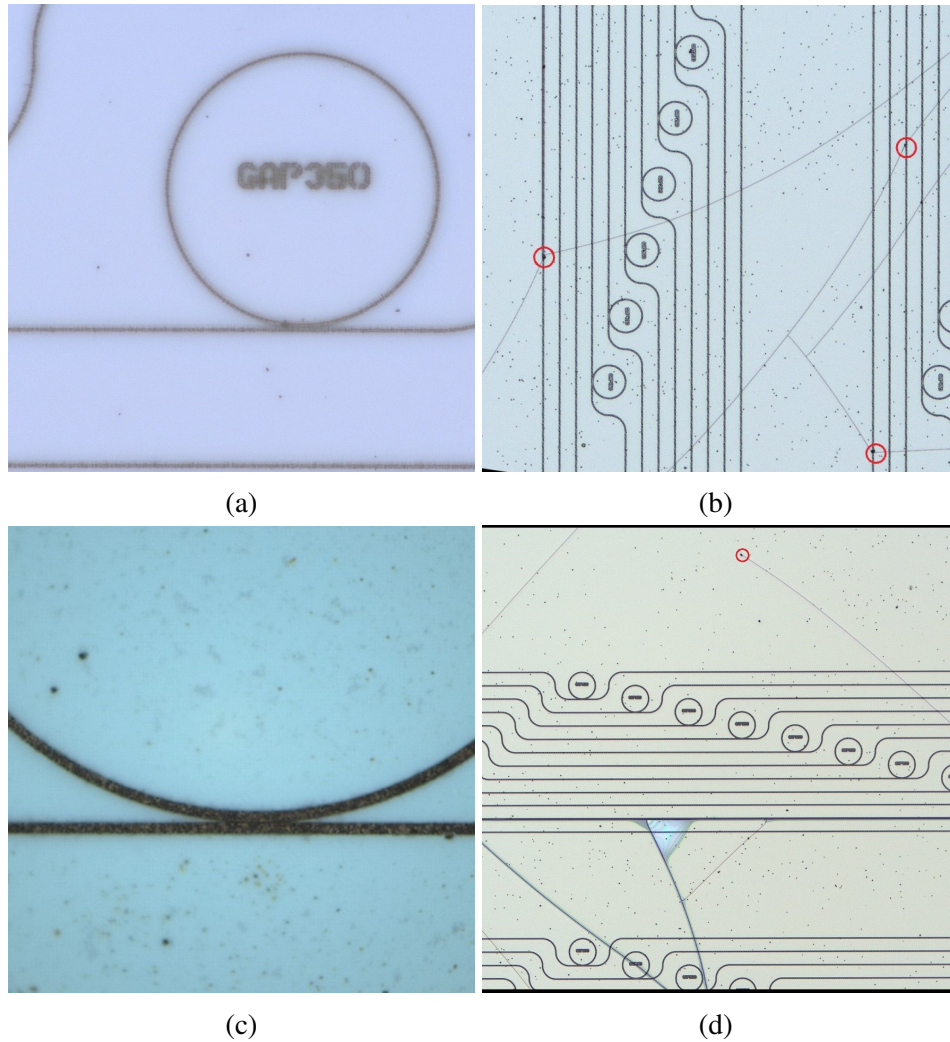


Figure 4.2: Laser microscope images of samples after annealing process. All the sample are annealed under the same circumstance. **a.** LS-CVD sample without top cladding. **b.** LS-CVD sample with TEOS top-cladding. **c.** PE-CVD sample without top cladding. **d.** PE-CVD sample with TEOS top-cladding. The cracks origin from contamination shown in **b** and **d**.

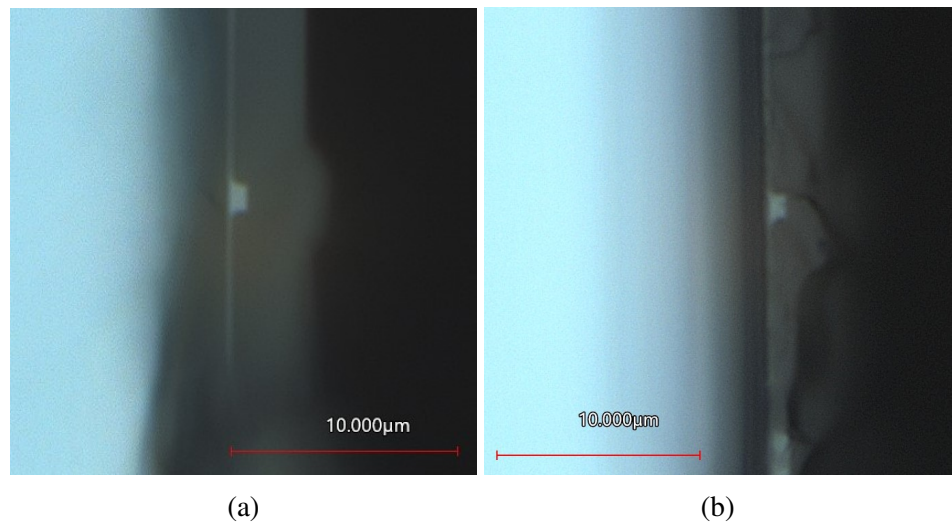


Figure 4.3: Microscope images of chip edge diced by laser dicing and manually cleaving. **a** Laser diced. **b** Manually cleaved. The scale in the images is 10 um.

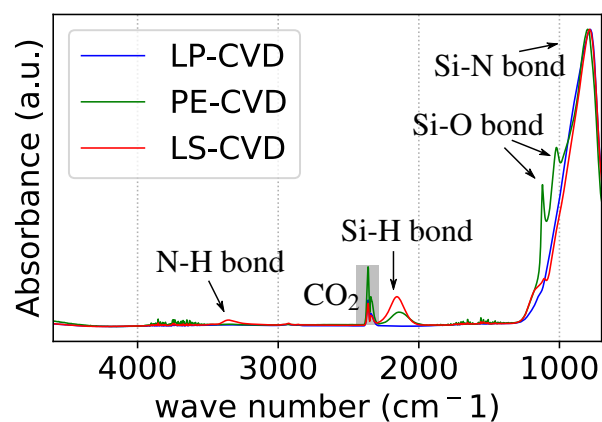


Figure 5.1: Absorbance of deposited film using Fourier-transform infrared spectroscopy. S-H and N-H bonds are obvious in LS-CVD and PE-CVD films.

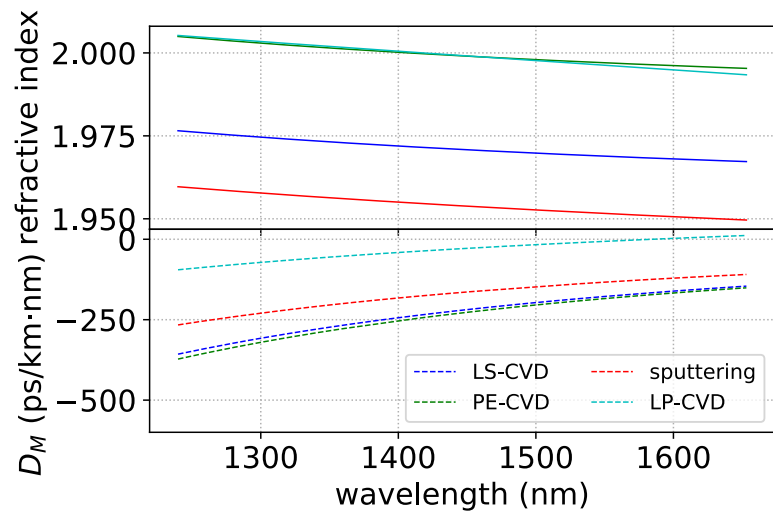


Figure 5.2: Refractive index and evaluated material dispersion of the film deposited measured via ellipsometry. The dispersion parameter is calculated by second-order difference of fitted Sellmeier equations.

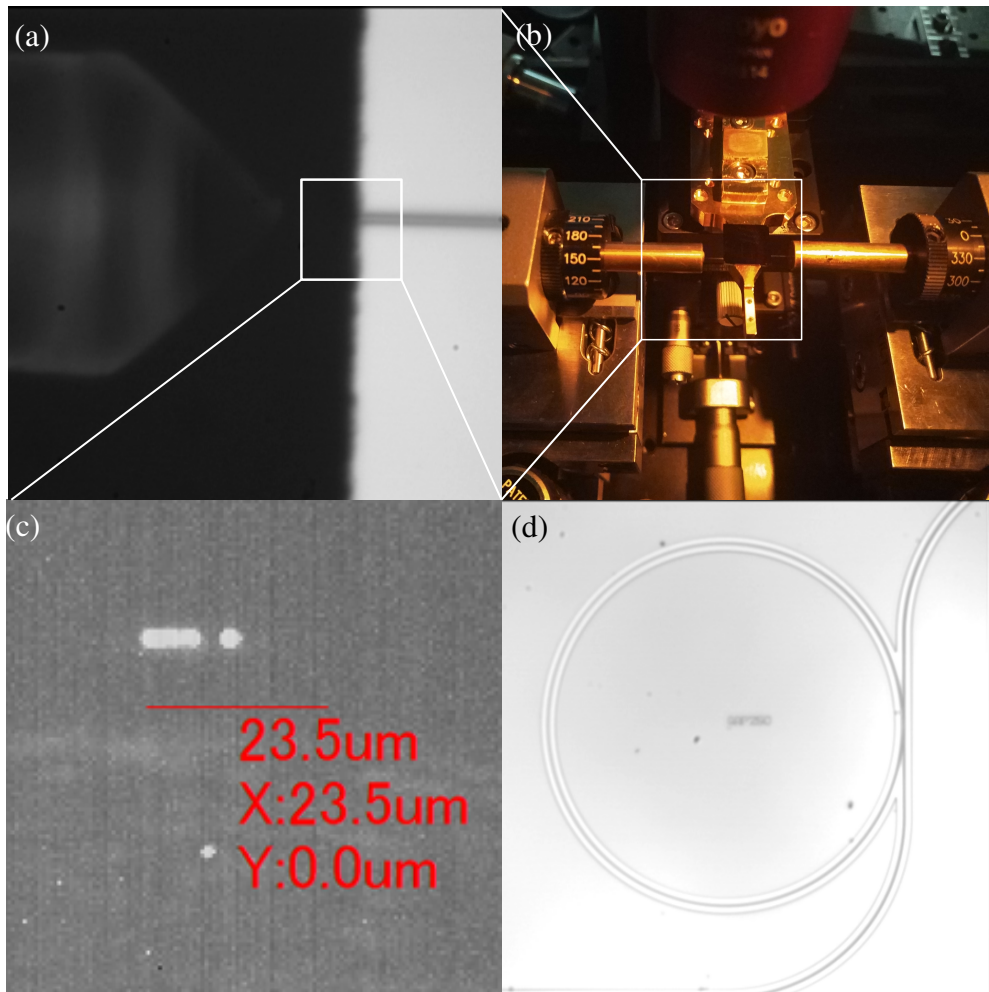


Figure 5.3: **Images of fiber launching setup.** **a** A lensed fiber is aligned to the end of bus waveguide. **b** Chip carried over a thermoelectric cooler. **c** Photo of waveguide end taken using infrared camera. **d** Optical microscope of fabricated sample.

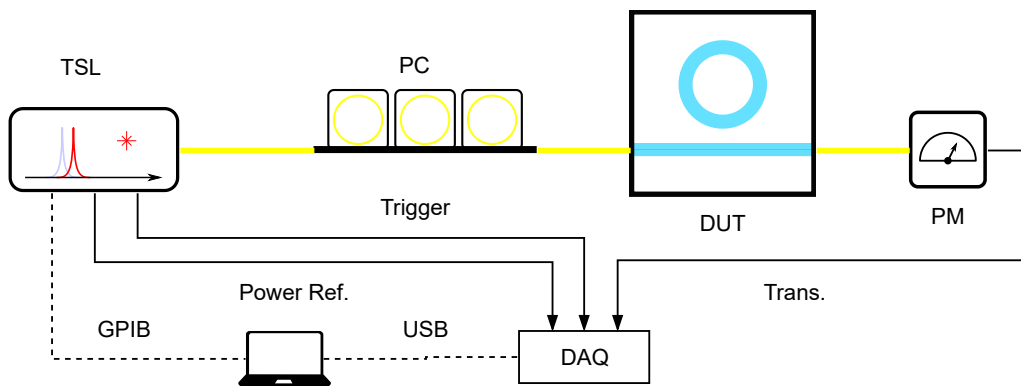


Figure 5.4: **Setup of transmission measurement system.** TSL, tunable semiconductor laser. PC, optical fiber polarization controller. DUT, device under test. PM, power meter. DAQ, data acquisition.

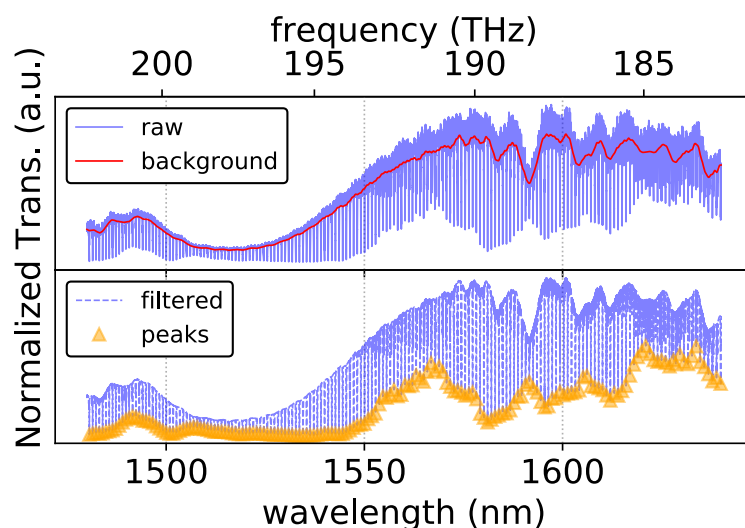


Figure 5.5: **Illustration of peaking searching.** The digital filter is used to process the raw transmission for better performance of peak searching algorithm.

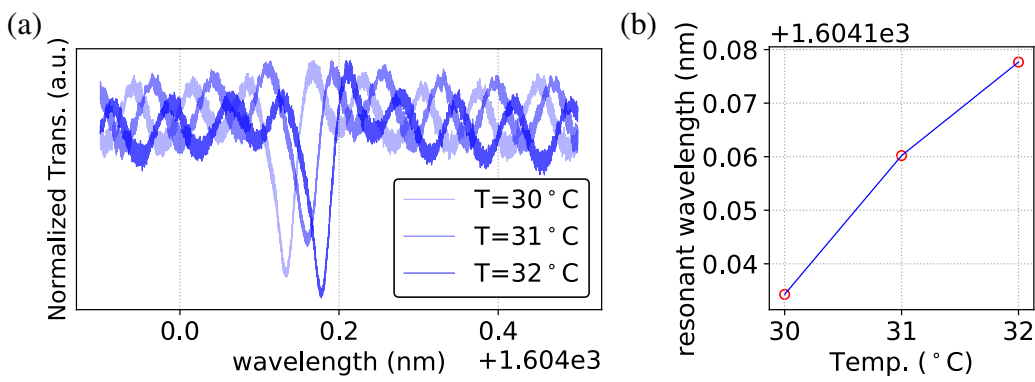


Figure 5.6: Thermal dependence of LP-CVD sample. **a.** Transmission measured at three temperatures. **b.** Resonant wavelengths extracted versus temperature. The estimated thermal dependence $d\lambda/dT$ is $23 \text{ nm}^{\circ}\text{C}$.

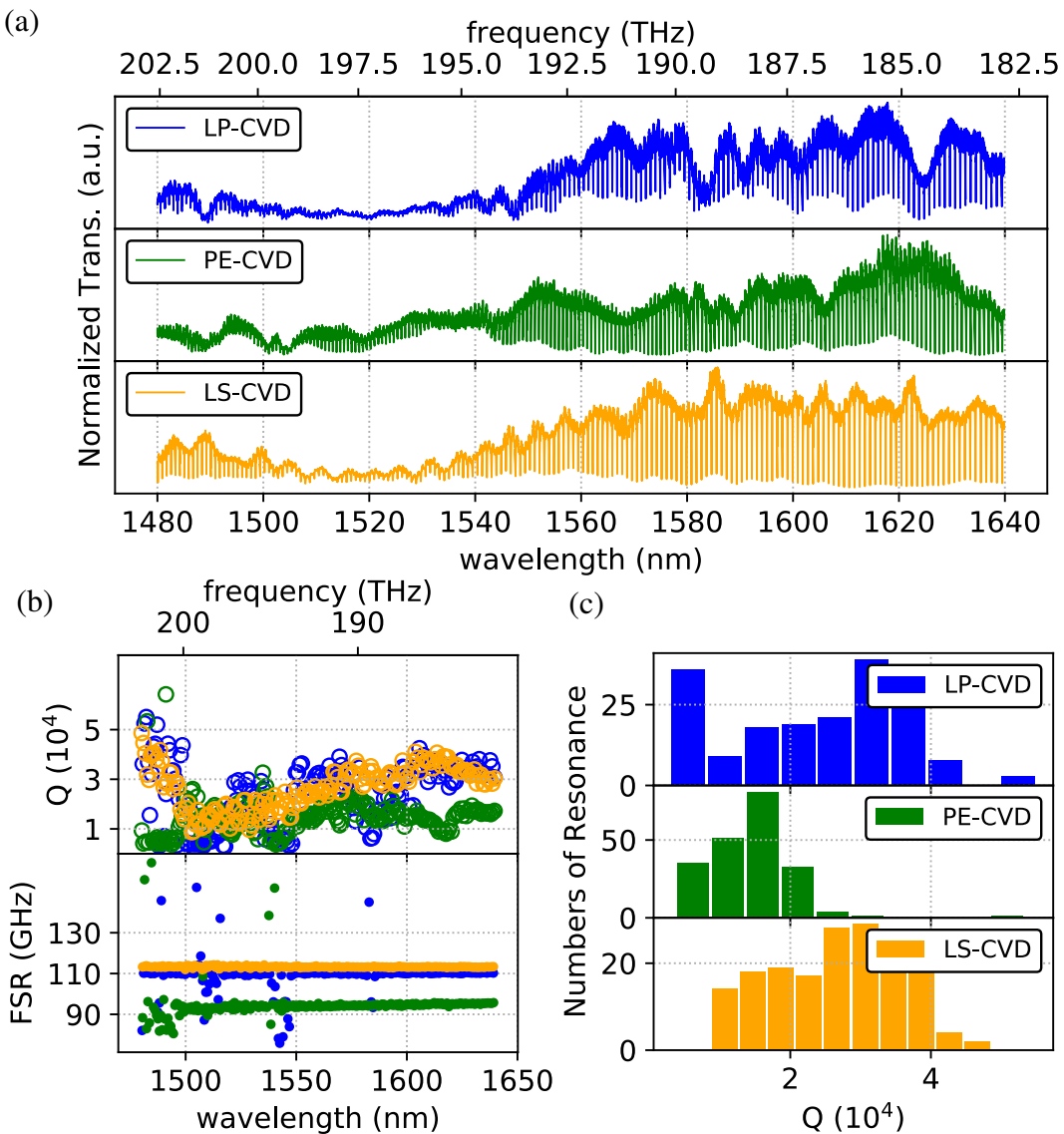


Figure 5.7: Comparison of device transmission, quality factors and FSR between three CVD methods. Identical ring resonators layout is used to fabricate all these samples, film thickness is 800 nm, ring width is 1.5 μm and ring radius is 200 μm .

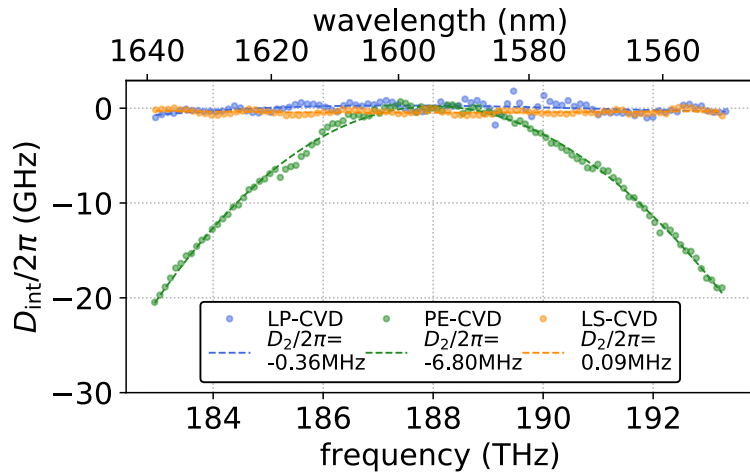


Figure 5.8: Integrated dispersion of devices fabricated using different CVD methods. Evaluated second-order dispersion of LP-CVD and LS-CVD devices presents near perfect dispersion compensation.

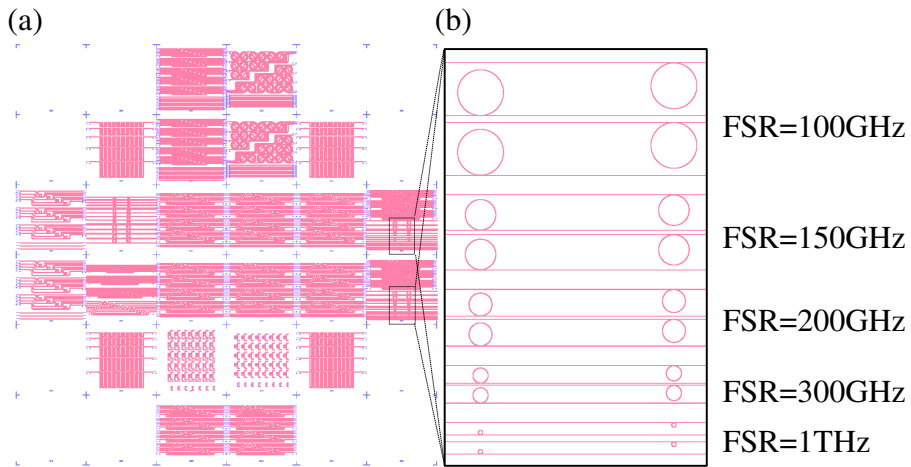


Figure 6.1: Layout of fabless samples. **a** is the layout of NTT-AT sample, including the identical design of LIGENTEC device shown in **b**. The cell size is $1\text{mm} \times 1\text{mm}$.

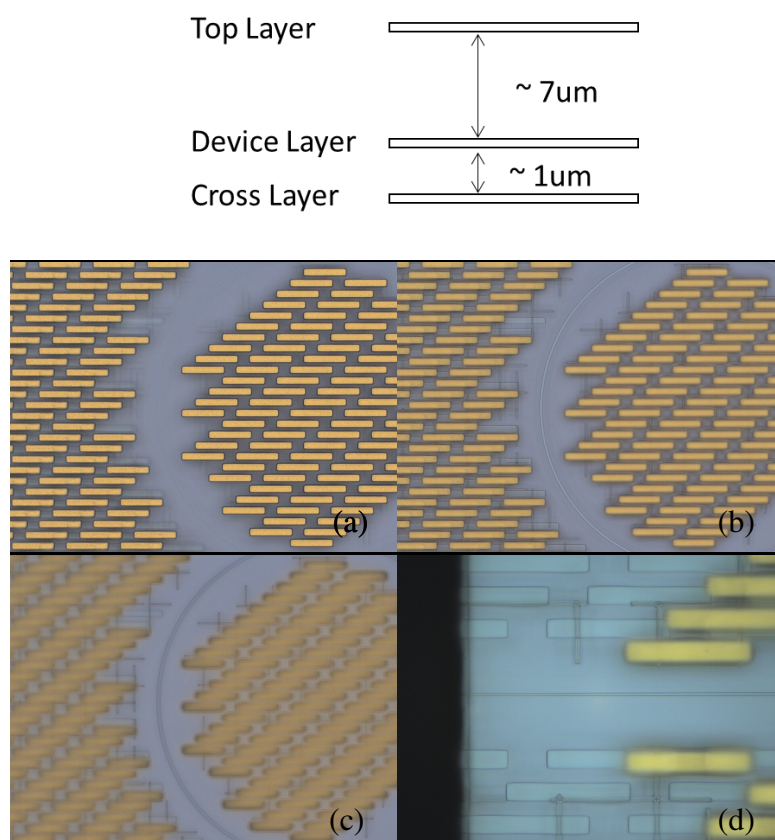


Figure 6.2: **Laser microscope images of LIGENTEC devices.** By lowering the focus depth, three layers are observed. **a.** Top metallic layer. **b.** Device layer. **c.** Crack stopper layer. **d.** Mode convertor. The metallic bar is 30 μm -long.

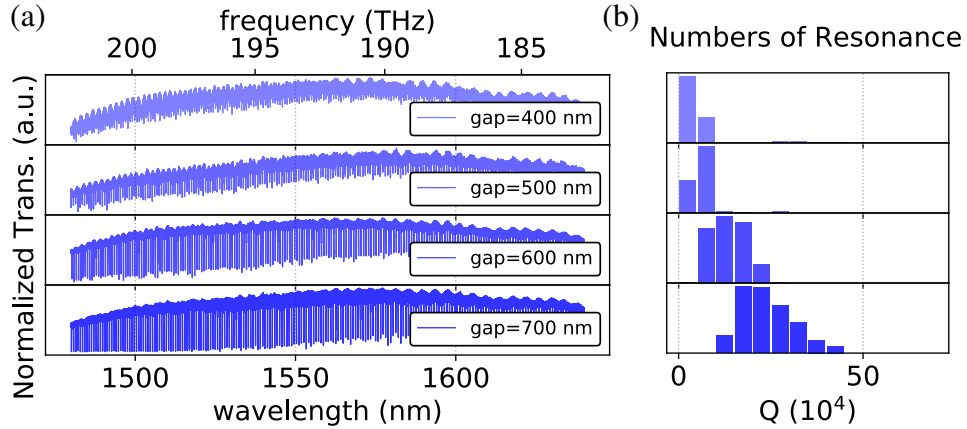


Figure 6.3: **Transmission and Q -factors of devices sweeping the gap.** The coupling condition varies from over coupling to critical coupling, as the negative prominence of resonance peak increases in **a**. The same tendency agrees with the Q -factors in **b**.

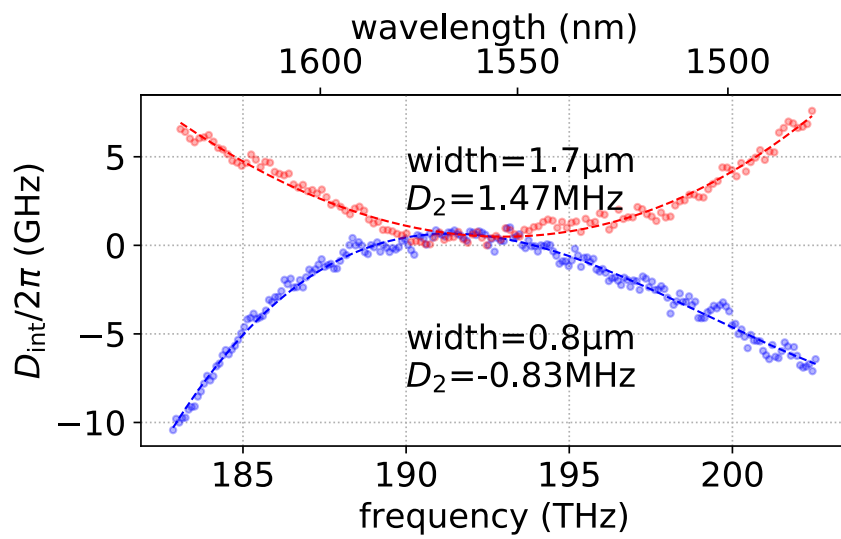


Figure 6.4: **Dispersion inversion shown by integrated dispersion.** With film thickness fixed at 0.8 μm , the ring width is tuned from 0.8 μm (Group 1) to 1.7 μm (Group 2) and the mode dispersion is inversed significantly.

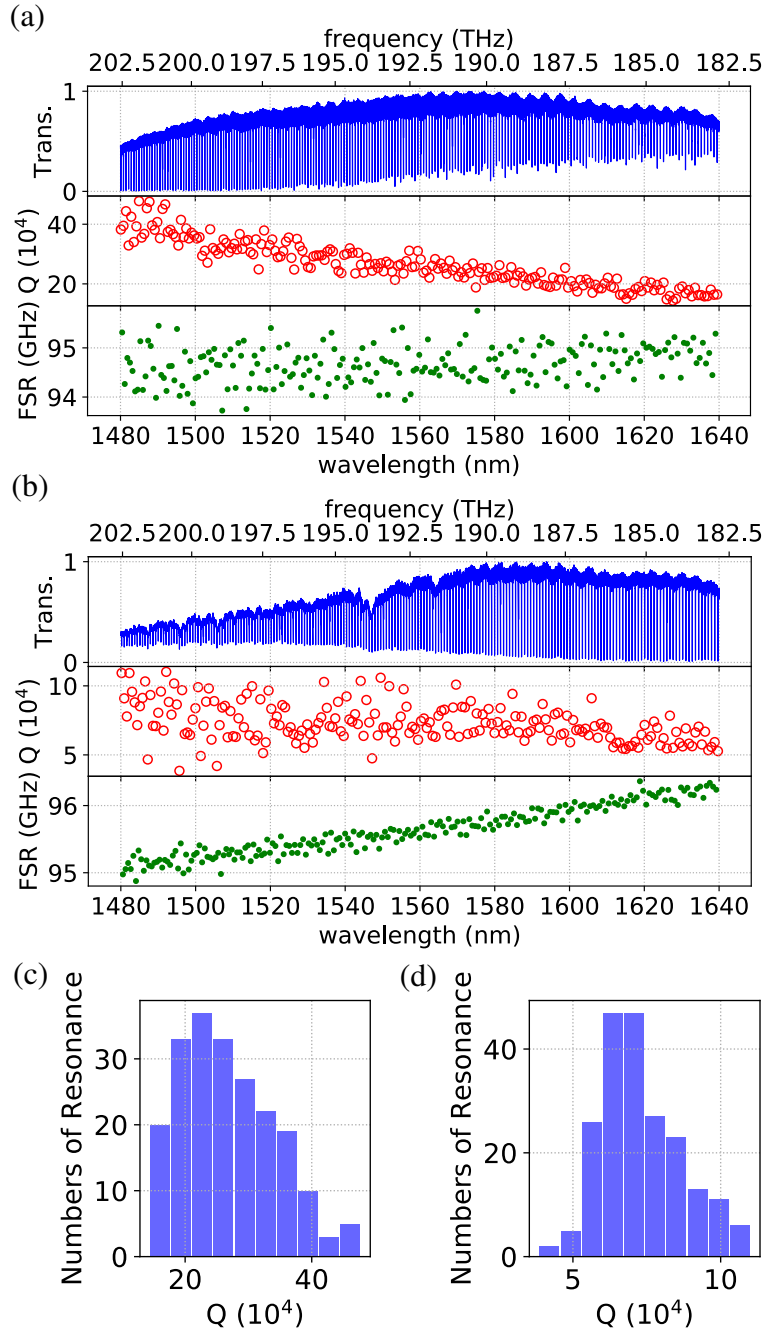


Figure 6.5: A comparison between identical ring resonator fabricated using LIGENTEC and NTT-AT technique. a. Transmission, Q -factors, FSR of LIGENTEC sample. b. Transmission, Q -factors, FSR of NTT-AT sample. Q -factors histogram of LIGENTEC and NTT-AT are given in c and d respectively. Identical pattern is used for fabrication (Group 1 Device 4, gap 700nm, FSR 100 GHz, ring width 0.8 μm).

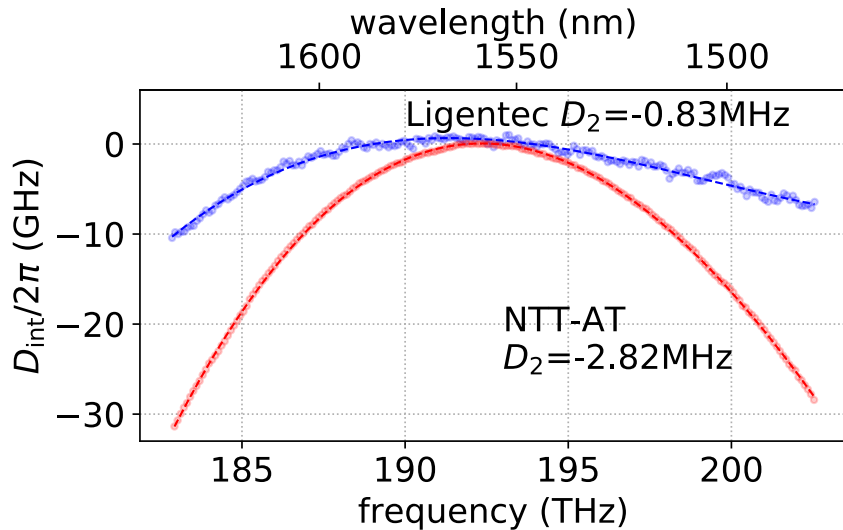


Figure 6.6: Comparison of integrated dispersion between LIGENTEC and NTT-AT samples with same device parameters. Fabrication process changes the dispersion effectively as a result of different film growing technology is performed.

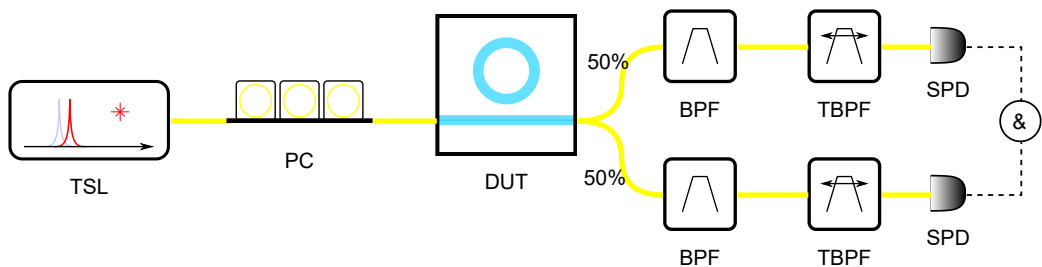


Figure 7.1: Setup of mode-resolvable singular photon pair generation. TSL, tunable semiconductor laser. PC, optical fiber polarization controller. DUT, device under test. BPF, band pass filter. TBPF, tunable band pass filter. SPD, single photon detector.

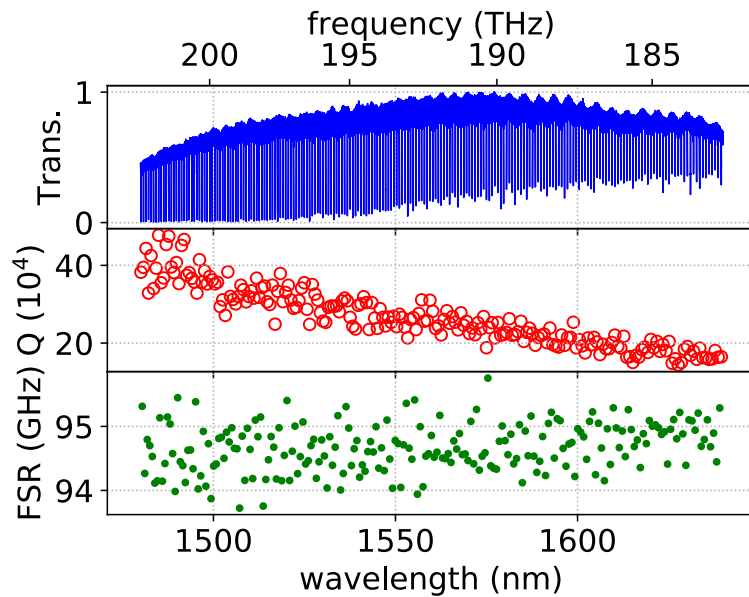


Figure 7.2: Transmission, quality factors and FSR of LIGENTEC Group 2 Device 1 employed in this chapter. $D_2 = 1.47$ MHz and Q -factor is around 2.5×10^5 in the filter band.

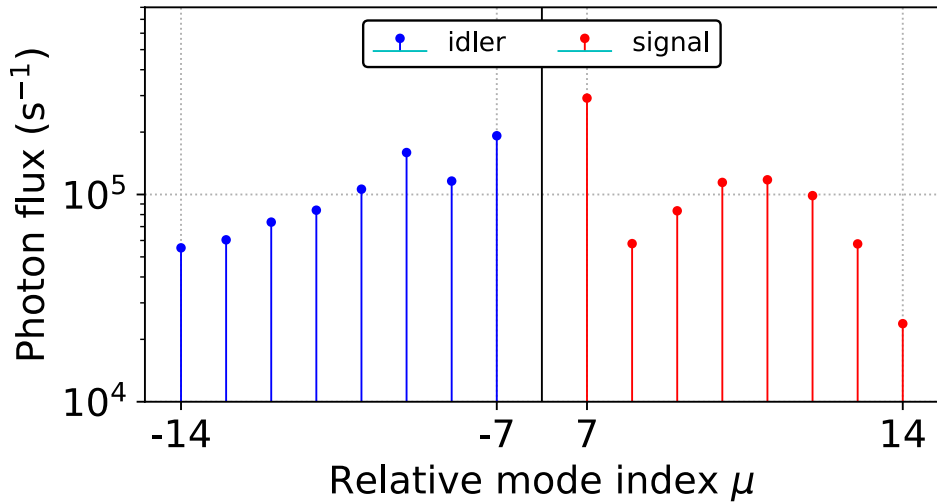


Figure 7.3: Photon flux with 100 μ W pump power. The pump power set as 100 μ W and central pump wavelength is at 1550.64 nm. Selected modes is from 1536 nm to 1544 nm for idler band and 1556 nm to 1564 nm for signal band.

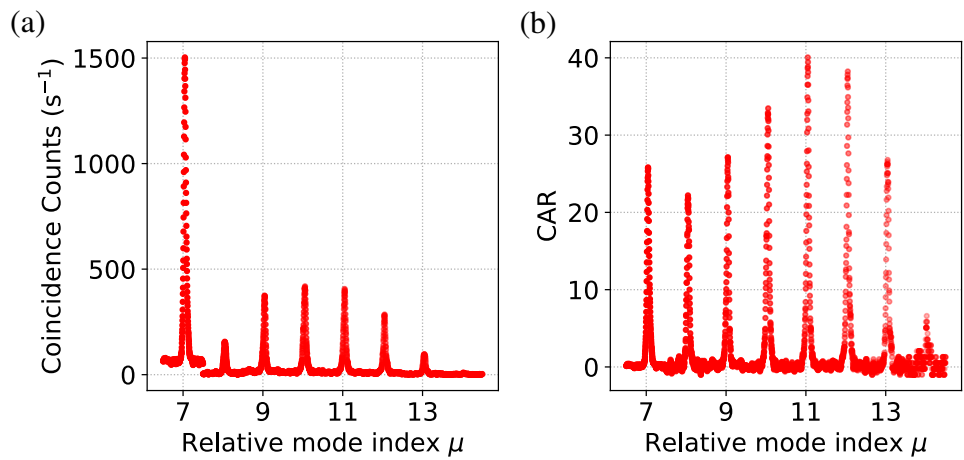


Figure 7.4: **Coincidence count and CAR at filtered modes.** Pump power is 100 μW . Coincidence window is 1 ns.

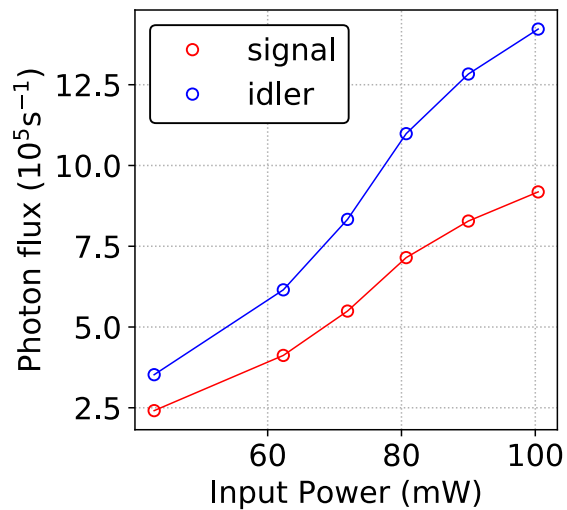


Figure 7.5: **Power dependence of photon fluxes during photon pair generation.** The input power is the power measured at the input port.

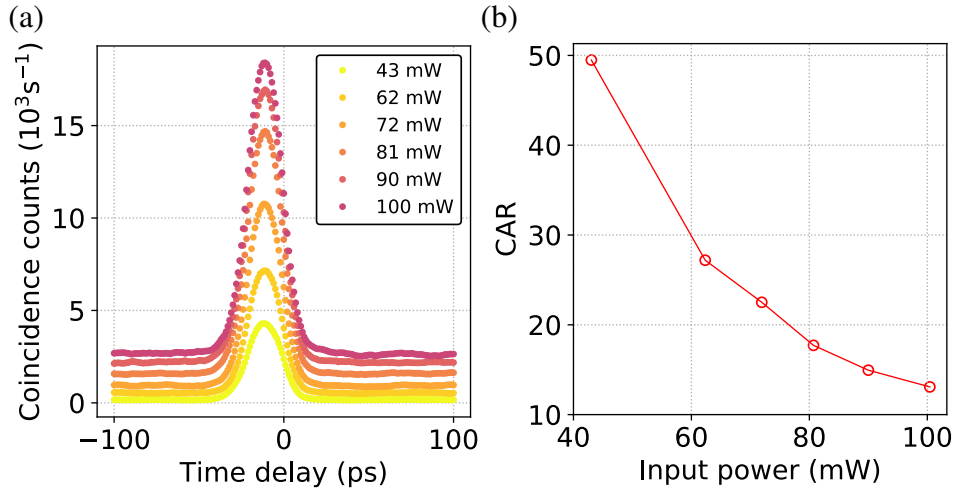


Figure 7.6: **Power dependence of coincidence count and coincidence-accidental count ratio during photon pair generation.** The input power is the power measured at the input port.

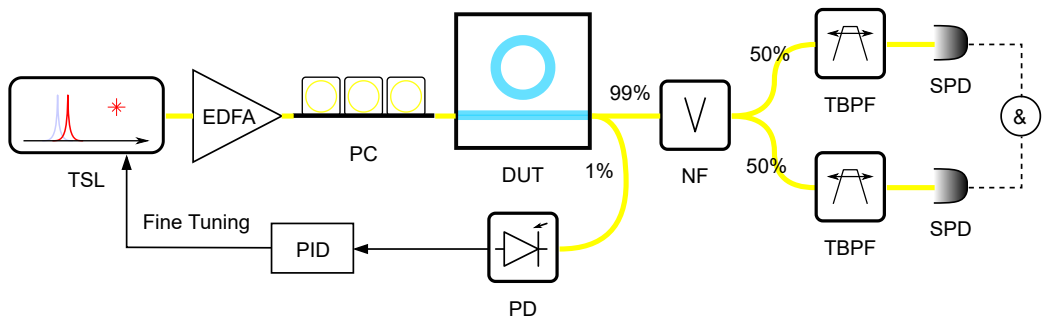


Figure 7.7: **Setup of long-time stable photon pair generation.** TSL, tunable semiconductor laser. PC, optical fiber polarization controller. DUT, device under test. NF, notch filter. TBPF, tunable band pass filter. SPD, single photon detector. PD, photodiode. PID, digital proportional–integral–derivative.

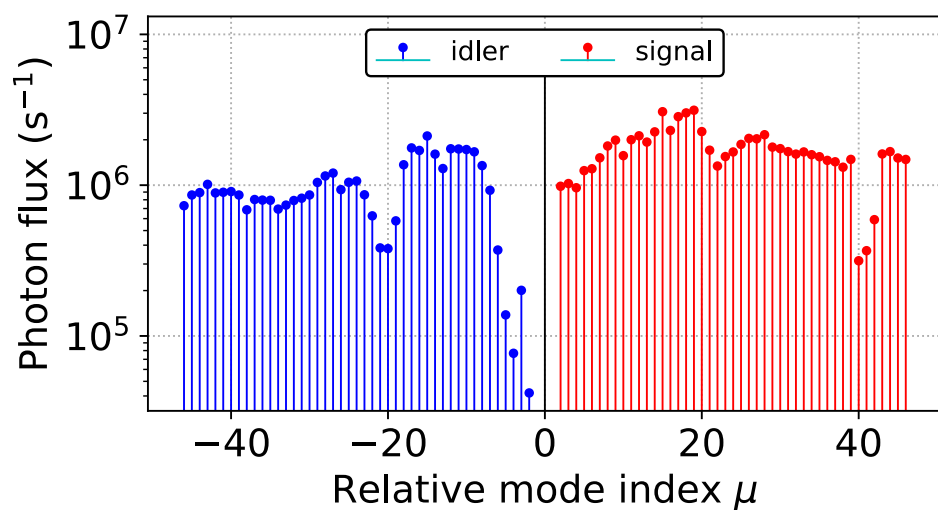


Figure 7.8: **Photon flux at 24.5 μW pump power of LIGENTEC Group 2 Device 1.** The mode near the central wavelength is effected by the notch filter.

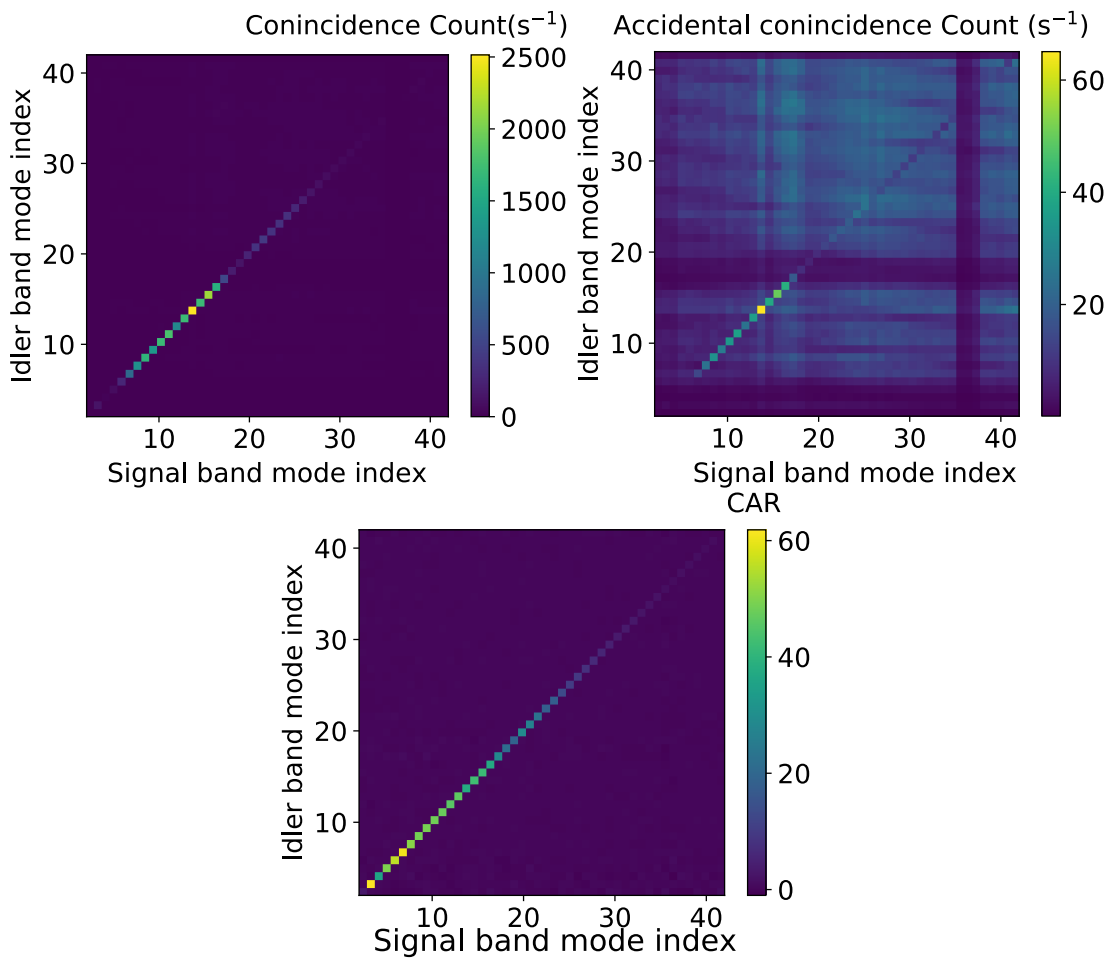


Figure 7.9: **Coincidence count, accidental coincidence count and coincidence-accidental count ratio used to evaluated joint spectral intensity.** The pump is 24.5 mW and the mode span corresponds to the range from 1499 nm to 1605 nm.

Table 1.1: **Comparison of several material properties between silicon and silicon nitride.** The data of silicon is cited from Reference [49] and silicon nitride refers to [34].

	silicon nitride	silicon
refractive index n at 1550 nm	1.9963	3.4757
transparent band	visible to NIR	NIR
two photon absorption β_{TPA} (cm/GW)	-	0.75
Kerr nonlinearity n_2 ($\text{m}^2 \text{ W}^{-1}$)	6.94×10^{-19}	5×10^{-18}

Table 4.1: **Recipes of CVD methods used in this research.** In the case of PE-CVD and LS-CVD, upper electrode and lower electrode are set at different temperature. RF power refers to radio frequency power used to excite the precursor gasses.

	LP-CVD	PE-CVD	LS-CVD
Facility	-	SAMCO PD-220NL	SMACO PD-100ST
Source	DCS:NH ₃ :N ₂ =6:5:189 sccm	SiH ₄ :NH ₃ :N ₂ =0.5:30 sccm	SN-2:N ₂ =0.5:30 sccm
Chamber Temp.	750°C-800°C	upper 150°C lower 350°C	upper 150°C lower 180°C
RF Power	-	40 W	30 W
Deposition Rate	-	15 nm/min	23 nm/min

Table 4.2: **Etching rate and selectivity of ICP process.** The etching rate is evaluated by step height measured via step profiler.

	Film Etching Rate (nm/min)	Resist Etching Rate (nm/min)	Selectivity
LP-CVD	19.20	12.76	1.50
PE-CVD	23.48	14.29	1.64
LS-CVD	27.40	2.08	13.17

Table 6.1: **Design parameters of LIGENTEC samples.** FSR is specialized at 1550 nm.

	Ring Radius (μm)	FSR (GHz)	Ring Width (μm)
Group 1	237.28	100	0.8
Group 2	157.95	150	1.7
Group 3	119.90	200	1.5
Group 4	78.55	300	1.7
Group 5	22.95	1000	1.7